NAVAL POSTGRADUATE SCHOOL

MONTEREY, CALIFORNIA

THESIS

FABRICATION OF SHAPE MEMORY ALLOYS USING AFFORDABLE ADDITIVE MANUFACTURING ROUTES

by

Farsai Anantachaisilp

December 2018

Thesis Advisor: Claudia C. Luhrs
Second Reader: Marcello Romano

THIS PAGE INTENTIONALLY LEFT BLANK

REPORT DOCUMENTATION PAGE			*Form Approved OMB No. 0704-0188*

1. AGENCY USE ONLY *(Leave blank)*	**2. REPORT DATE** December 2018	**3. REPORT TYPE AND DATES COVERED** Master's thesis

4. TITLE AND SUBTITLE FABRICATION OF SHAPE MEMORY ALLOYS USING AFFORDABLE ADDITIVE MANUFACTURING ROUTES	**5. FUNDING NUMBERS** NPS-18-N337-A
6. AUTHOR(S) Farsai Anantachaisilp	
7. PERFORMING ORGANIZATION NAME(S) AND ADDRESS(ES) Naval Postgraduate School Monterey, CA 93943-5000	**8. PERFORMING ORGANIZATION REPORT NUMBER**
9. SPONSORING / MONITORING AGENCY NAME(S) AND ADDRESS(ES) N/A	**10. SPONSORING / MONITORING AGENCY REPORT NUMBER**

11. SUPPLEMENTARY NOTES The views expressed in this thesis are those of the author and do not reflect the official policy or position of the Department of Defense or the U.S. Government.

12a. DISTRIBUTION / AVAILABILITY STATEMENT Approved for public release. Distribution is unlimited.	**12b. DISTRIBUTION CODE** A

13. ABSTRACT (maximum 200 words)

The primary objective of this research was to develop paste formulations to enable the fabrication of shape memory alloys (SMA) using low-cost additive manufacturing routes. We focused on determining which precursor particulates, binding agents and post-processing conditions could sinter the 3D printed parts. Nickel-titanium nano/micron-sized particulates along paraffin/alcoholic gel binders were tested as raw materials to produce pastes. Scanning electron and optical microscopy, energy dispersive spectroscopy and X-ray diffractometry were employed to determine the microstructural features in the raw material and final products. Thermal treatments to sinter the parts were performed in a tube furnace or a hot isostatic press. It was found that it is possible to 3D print metal pastes using micrometric particles, gel binders and a modified low-cost polymeric printer. Nanoparticle formulations were found to behave as shear thinning fluids and are not recommended for this application. The post-processing conditions that were successful creating sintered structures used 1000℃ and pressures above 138MPa. The Ni-Ti phases generated deviated from the ideal NiTi stoichiometry, however, were close to those found in commercially available SMA wires. SMAs could be employed to produce actuators and deployment mechanisms in space applications. This research introduces a novel way to fabricate SMAs that could reduce costs and widen the environments where their production could take place.

14. SUBJECT TERMS shape memory alloy, additive manufacturing, paste formulations, NiTi	**15. NUMBER OF PAGES** 89
	16. PRICE CODE

17. SECURITY CLASSIFICATION OF REPORT	**18. SECURITY CLASSIFICATION OF THIS PAGE**	**19. SECURITY CLASSIFICATION OF ABSTRACT**	**20. LIMITATION OF ABSTRACT**
Unclassified	Unclassified	Unclassified	UU

NSN 7540-01-280-5500 Standard Form 298 (Rev. 2-89) Prescribed by ANSI Std. 239-18

THIS PAGE INTENTIONALLY LEFT BLANK

Approved for public release. Distribution is unlimited.

FABRICATION OF SHAPE MEMORY ALLOYS USING AFFORDABLE ADDITIVE MANUFACTURING ROUTES

Farsai Anantachaisilp
Lieutenant, United States Navy
BS, U.S. Naval Academy, 2012

Submitted in partial fulfillment of the
requirements for the degree of

MASTER OF SCIENCE IN ASTRONAUTICAL ENGINEERING

from the

NAVAL POSTGRADUATE SCHOOL
December 2018

Approved by: Claudia C. Luhrs
Advisor

Marcello Romano
Second Reader

Garth V. Hobson
Chair, Department of Mechanical and Aerospace Engineering

THIS PAGE INTENTIONALLY LEFT BLANK

ABSTRACT

The primary objective of this research was to develop paste formulations to enable the fabrication of shape memory alloys (SMA) using low-cost additive manufacturing routes. We focused on determining which precursor particulates, binding agents and post-processing conditions could sinter the 3D printed parts. Nickel-titanium nano/micron-sized particulates along paraffin/alcoholic gel binders were tested as raw materials to produce pastes. Scanning electron and optical microscopy, energy dispersive spectroscopy and X-ray diffractometry were employed to determine the microstructural features in the raw material and final products. Thermal treatments to sinter the parts were performed in a tube furnace or a hot isostatic press. It was found that it is possible to 3D print metal pastes using micrometric particles, gel binders and a modified low-cost polymeric printer. Nanoparticle formulations were found to behave as shear thinning fluids and are not recommended for this application. The post-processing conditions that were successful creating sintered structures used 1000℃ and pressures above 138MPa. The Ni-Ti phases generated deviated from the ideal NiTi stoichiometry, however, were close to those found in commercially available SMA wires. SMAs could be employed to produce actuators and deployment mechanisms in space applications. This research introduces a novel way to fabricate SMAs that could reduce costs and widen the environments where their production could take place.

THIS PAGE INTENTIONALLY LEFT BLANK

TABLE OF CONTENTS

I. INTRODUCTION....1
A. STATE-OF-THE-ART OF ADDITIVE MANUFACTURING....2
B. BACKGROUND....4
1. History and Overview of Shape Memory Alloys....4
2. Fabrication Routes for NiTi Alloys....8
C. OBJECTIVES....10

II. EXPERIMENTAL METHODS....13
A. FABRICATION....15
1. Paste Formulations....15
2. 3D Printing Conditions....18
3. Thermal Treatment....21
B. MATERIALS CHARACTERIZATION....26
1. Scanning Electron Microscopy/ Energy Dispersive Spectroscopy....26
2. Simultaneous Thermal Analysis (STA)....28
3. X-ray Diffraction....28
4. Optical Microscopy....30

III. RESULTS....31
A. PASTE FORMULATIONS DEVELOPMENT....31
1. Commercial PLA with Fillers....32
2. Semi-solid, Saturated Hydrocarbon Paraffin....36
3. Alcohol-based Gel....39
B. POST-TREATMENTS OF 3D PRINTS....45
1. Furnace....45
2. Hot Isostatic Pressing....53

IV. CONCLUSION....61
A. MILESTONES ACHIEVED....61
B. FUTURE DIRECTIONS....63

LIST OF REFERENCES....65

INITIAL DISTRIBUTION LIST....69

THIS PAGE INTENTIONALLY LEFT BLANK

LIST OF FIGURES

Figure 1. 3D Computer-Aided Design Model (Using Fusion 360 Software) of a Tensile Bar 2

Figure 2. Classification of Methods for Manufacturing Metals Starting from Powder 3

Figure 3. Superelasticity Process. Source: [13]. 5

Figure 4. Demonstration of the Shape Memory Effect 6

Figure 5. NiTi Phase Diagram. Source: [17]. 8

Figure 6. Frangibolt Actuator. Source: [19]. 11

Figure 7. Cord-Cutting Module Using SMA Wire. Source: [20]. 11

Figure 8. Opening Sequence of the Solar Sail Using SMAs. Source: [18]. 12

Figure 9. Flowchart of Experimental Approach 14

Figure 10. Tensile Testing System 15

Figure 11. FlackTek SpeedMixer 16

Figure 12. Droplet of a Mixture on Sample Holder 18

Figure 13. 3D Model of a Tensile Bar 19

Figure 14. Plastic Tubing Inserted with Nozzle Tip Attached Through an Adaptor Clip 20

Figure 15. Polypropylene Nozzle Tips 20

Figure 16. Setup of the 3D Printer 21

Figure 17. Furnace Setup 22

Figure 18. Heating Conditions Plot of Sample 1 23

Figure 19. HIP Conditions for Sample 1 (top), Sample 2 (middle), and Sample 3 (bottom) 25

Figure 20. SEM-EDS Instrument 26

Figure 21. Illustration of Secondary Electron Emission. Source: [27]. 27

Figure 22. DSC/TG Instruments 28
Figure 23. X-ray Diffractometer 29
Figure 24. XRD Sample Preparation Process 30
Figure 25. Results and Discussions Layout....31
Figure 26. Results from Tensile Tests....32
Figure 27. Microscopy Images of the Copper-PLA After Post-Treatment....33
Figure 28. Microscopy Images of (a) Copper part that oxidized produced from a PLA-Cu filament and (b) Carbon residue observed in a PLA-Cu filament sample that was annealed using inert atmosphere....34
Figure 29. SEM Images of Raw Powders: (a) Ti (45μm), (b) Ni (nano), (c) Ni (5μm)....35
Figure 30. TG Comparison of Samples in Different Gas Atmosphere 36
Figure 31. (a) SEM Image and (b) EDS Analysis of Ti-64 and Paraffin Under Nitrogen 37
Figure 32. SEM Image of Ti-64 and Paraffin under Argon 38
Figure 33. XRD Pattern of Ti-64 sample mixed with paraffin and heat treated to 1000°C using Argon atmosphere 38
Figure 34. XRD Pattern of Mixed Ti (45 μm) and Ni (nano) Powder with Gel 40
Figure 35. A 3D Printed Part....40
Figure 36. Mixture of Gel with (a) Ni (nano), (b) Ni (5 μm)....41
Figure 37. Viscosities of Samples Containing Ti (micron) and Ni (nano and micron) Particles vs. Shear Rate 42
Figure 38. Shear Stress of Samples Containing Ti (micron) and Ni (nano and micron) Particles vs. Shear Rate 43
Figure 39. Viscosity of Samples Containing Pure Gel Only or Gel with Ni (nano or micron) vs. Shear Rate 44
Figure 40. Shear Stress of Samples Containing Pure Gel Only or Gel with Ni (nano or micron) vs. Shear Rate 44

Figure 41. Sample Containing 20% Ni (5 μm) and 80% Gel after Sintering at Magnification of (a) 300x and (b) 1000x....45

Figure 42. EDS Plot of Sample Containing 20% Ni (5 μm) and 80% Gel After Furnace....46

Figure 43. SEM Image of Sample 40% Ni (5 μm) and 60% Gel at Magnification (1000x)....47

Figure 44. EDS Plot of Sample Containing 40% Ni (5 μm) and 60% Gel after Furnace....47

Figure 45. Sample Containing 33% Ni (nano)-Ti (45 μm) and 67% Gel (a) Prior to Sintering and (b) after Sintering....48

Figure 46. XRD Pattern of Sample Containing 33% Ni (nano)-Ti (45 μm) and 67% Gel After Sintering....49

Figure 47. Sample Containing 33% Ni(nano)-Ti (45 μm) and 67% Gel: EDS Plot (left) and SEM Image at 1000x Magnification (right)....50

Figure 48. Commercial Nitinol Wire at Magnification of: (a) 70x, (b) 5000x....50

Figure 49. EDS Analysis of Commercial Nitinol Sample....51

Figure 50. DSC Comparison of Commercial Nitinol Wire and Sample Containing 33% Ni (nano)-Ti (45 μm) and 67% Gel....52

Figure 51. 3D Printed Samples Containing Ni (5 μm), Ti (45 μm) and Gel....53

Figure 52. Returned HIPped Samples Containing Ni (5 μm), Ti (45 μm) and Gel....54

Figure 53. Cold-Mounted HIPped Samples Containing Ni (5 μm), Ti (45 μm) and Gel Treated at Pressure: 138 and 172 MPa (20k and 25k psi)....55

Figure 54. SEM Images of HIPped Samples Containing Ni (5 μm), Ti (45 μm) and Gel Treated at Pressure of (a) 138 MPa, (b) 172 MPa....55

Figure 55. Sample Containing Ni (5 μm), Ti (45 μm) and Gel Treated at 138 MPa in (a) Raw Optical Image and (b) Binary Image....56

Figure 56. Specimen Treated at 172 MPa in (a) Raw Optical Image and (b) Binary Image....56

Figure 57. SEM Image of HIPped Samples Treated at 138 MPa (top) and 172 MPa (bottom)....57

Figure 58. Samples Containing CNTs, Ni (5 μm), Ti (45 μm) and gel Prior to (left) and After HIPped at 207 MPa (right) 58

Figure 59. Prepared Sample Containing CNTs, Ni (5 μm), Ti (45 μm) and Gel Treated at 207 MPa for Characterization.....59

Figure 60. SEM Images of HIPped Sample Containing CNTs, Ni (5 μm), Ti (45 μm) and Gel at Magnification of 300X (left) and 1000X (right).....59

LIST OF TABLES

Table 1. Comparison of Different NiTi Manufacturing Methods. Adapted from [7]. 9

Table 2. Samples Tested in a Rheometer 17

Table 3. Cura Print Setup for Tensile Bar 19

Table 4. Different Compositions and Furnace Conditions of Various Samples. 23

Table 5. Different Compositions and HIP Conditions of Various Samples. 24

THIS PAGE INTENTIONALLY LEFT BLANK

LIST OF ACRONYMS AND ABBREVIATIONS

3DP	three dimensional printing
AIP	American Isostatic Pressing, Inc.
AM	additive manufacturing
Ar	argon
CNT	carbon nanotube
CS	conventional sintering
DSC	differential scanning calorimetry
EDS	energy dispersive x-ray spectroscopy
HIP	hot isostatic pressing
µm	micrometer
N_2	nitrogen
Ni	nickel
NiTi	nickel-titanium alloy (or solid solution)
nm	nanometer
NPS	Naval Postgraduate School
PLA	polylactic acid
PM	powder metallurgy
PP	polypropylene
SEM	scanning electron microscope
SMA	shape memory alloy
SME	shape memory effect
STL	stereolithography
TG	thermogravimetric
Ti	titanium
Ti-64	Ti-6Al-4V
XRD	x-ray diffraction

THIS PAGE INTENTIONALLY LEFT BLANK

ACKNOWLEDGMENTS

First and foremost, I would like to thank my thesis advisor, Dr. Claudia Luhrs, for imparting valuable knowledge and guiding me through my research. Your dedication and expertise in this subject helped me to complete my graduate-level research; not only that, you also inspired me to take those initial steps to pursue new ideas and extend my scope of knowledge. You pushed me hard from the beginning to the end, and I am truly grateful for this because you made it possible for me to accomplish my thesis research.

I would also like to thank Dr. William Wu for all the trainings and support in the characterization process throughout my research. You were always there when I needed your help.

Additionally, I want to acknowledge Professor Joaquin Tirano from National University of Colombia for conducting the rheometry measurements presented in Chapter II. Also, many thanks go to CDR Brian Earp and LT Alex Roman for their roles in assisting me with the final project related to my thesis topic in ME4901 Nanomaterials course.

Finally, I would like to express my utmost gratitude to the most important person in my life, my husband, Thomas. Thank you for your unwavering support and encouragement through all the challenging times and long hours spent on my research and schoolwork. You are always patient, loving, and caring for me through it all. You never failed to give me comfort and words of encouragement and sometimes even tutored me. You are an incredible man! None of my accomplishments would be possible without you.

THIS PAGE INTENTIONALLY LEFT BLANK

I. INTRODUCTION

The emerging field of additive manufacturing (AM) has gained significant attention in both industry and academia. In 2015, the market share of three dimensional printing (3DP) raised to $5.2 billion, and was estimated to increase as much as $30 billion in 2022 [1]. The demand for additively manufactured metals and alloys is rapidly rising, at a pace greater than polymeric AM. The number of metal AM systems sold in 2016 and 2017 raised nearly 80% in a single year [2]. Many engineers are starting to explore how to use AM with wide range of metallic materials such as titanium, aluminum, and nickel-titanium (NiTi) alloys. There is even greater emphasis on a production of complex alloy shapes such as hollow, lattice-like or truss-based structures with the potential use in medical and space applications [3]. This opens the door for innovative and new actuator designs which can offer mechanical robustness and various functionality.

The essence of AM technology involves depositing materials layer by layer based on computer-aided design (CAD), which is also known as 3DP, represented in Figure 1. This technique offers great potentials such as, limitless geometric flexibility, short lead times and non-necessity of complex tools [2]. In contrast with subtractive manufacturing technologies, AM uses only the necessary amount of materials to produce the parts. All of those attributes can optimize cost, time and material effectiveness in the overall production. The concept of 3DP originated in the 1980s from a stereo-lithography (STL) process [4]. In those days, the most popular choice of material in 3DP has been different types of thermoplastic polymers [4]. These polymers were utilized in 3DP to build parts from the bottoms up by heating the thermoplastic to a semi-liquid state and extrude it along an STL-defined extrusion path.

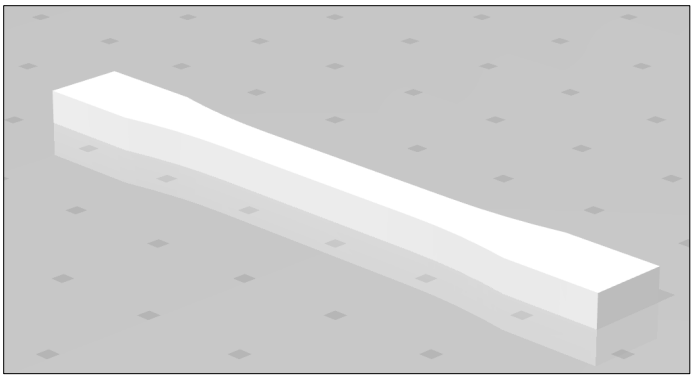

Figure 1. 3D Computer-Aided Design Model (Using Fusion 360 Software) of a Tensile Bar

A. STATE-OF-THE-ART OF ADDITIVE MANUFACTURING

A range of manufacturing methods for producing metals currently exist, including casting and powder metallurgy (PM). Casting technique involves high temperature melting of materials that get deposited into a mold of the desired shape that is then allowed to solidify. Casted parts could present irregularities transferred from imperfections in the mold, have an increased impurity pickup and required surface post-processing [3]. Metals can also be produced by PM, which refers to techniques that allow the fabrication of consolidated parts from metal powders. Through conventional PM process, raw powders are compressed into the desired shape, resulting in a "green" compact which is then annealed in controlled atmospheres to gain the desired density and reduced porosity. According to Sina et al., PM route can help minimize segregation effects by allowing materials to deposit close to the desired compositions [5]. Thus, using the PM processing route makes it possible to produce near net (close to final) shape components of SMA with desired quality, reducing the need for surface finishing. Other "advantages include avoiding expensive thermomechanical working, the machining of cast alloys and high losses of materials" [6]. In comparison with casting approaches, PM offers more capabilities and fewer limitations in terms of synthesizing the material. PM has been known to produce up to 50% porosity through the sintering process, however the desired levels of porosity in the product can be obtained by controlling the compaction pressure and sintering time [7].

Figure 2 lists the current powder metallurgy approaches, on the right side highlighting the processes traditionally used and on the left side the new additive manufacturing techniques.

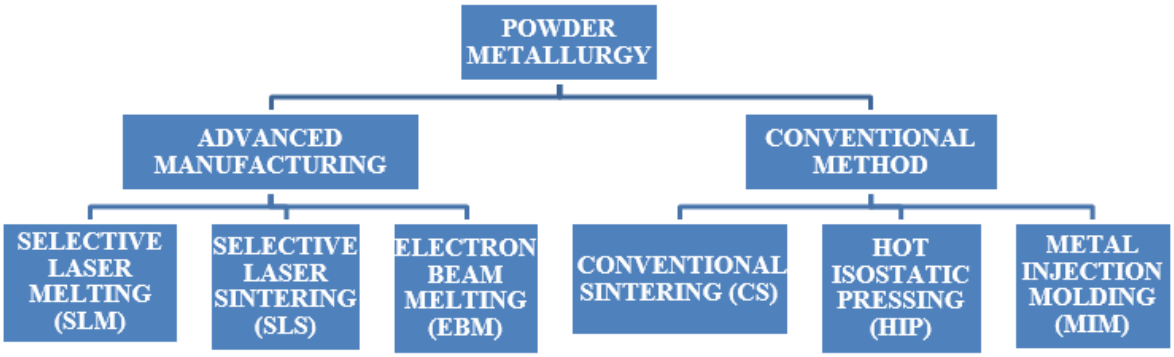

Figure 2. Classification of Methods for Manufacturing Metals Starting from Powder

Among powder-based AM processes, the most commonly used manufacturing methods are Selective Laser Melting (SLM), Selective Laser Sintering (SLS) and Electron Beam Melting (EBM) [7]. These methods are categorized as advanced manufacturing, but are also performed by joining materials layer by layer. They used powder as the raw material in the process, and the laser or electron beam is used to melt the powder layer selectively based on the sliced CAD information. SLM of metallic powders is based on a complete melting mechanism, whereas SLS requires a partial melting of powder [8]. By contrast, the EBM utilized the electron beam as the energy source in the process, and the entire system is protected from oxidation vacuum chamber [9]. These methods are considered to have remarkable potentials in producing shape memory objects of NiTi, but the biggest drawback with these powder/laser-based AM processes is their high production cost. The machines used in these processes require high energy and relatively complex to operate.

Comparing to the advanced manufacturing methods, the conventional methods such as metal injection molding (MIM) can be highly appealing in terms of affordability

and simple operation, however are limited in the size and shape that can be attained. Post-treatments are necessary to achieve sintering that will produce parts with reduced porosity and the desired mechanical properties. These methods do require post-processing for surface treatment and dimensional accuracy. However, these conventional methods hold promising potential for creating metals or alloys without the need of e-beam or laser technologies.

Currently, all the available commercial powders used for PM and AM processes have particle size distributions from tenths to hundreds of micrometers. For this reason, the size of the features that can be achieved are limited. Thus, smaller micron particles or nanoparticles (size of 100 nm or less) could be the ultimate solution to this concern, based on the fact that they are known to have higher reactivity; their higher levels of surface area and surface energy promote sintering at lower temperatures.

B. BACKGROUND

The concept of using small particulates of either pure metal or alloy metal powder to produce larger components is not novel. In fact, the technology of PM can be traced back to early civilizations. Nowadays, PM technology is utilized and implemented to broaden the spectrum of metals available for different applications including the electronic, medical, and in particular, the space industries.

Specifically, NiTi is an attractive alloy in the space and other engineering applications due to its unique functional and mechanical properties. It exhibits shape memory effect (SME), superelasticity and corrosion characteristics, low stiffness, damping behaviors, and biocompatibility.

1. History and Overview of Shape Memory Alloys

Since the early 1930s, the discovery of SME was first found by the chemist, A. Olander. He initially discovered the pseudoelastic behavior in Au-47.5at% Cd alloy [10]. Later in 1938, Greninger and Mooradian observed the basic phenomenon of the formation and disappearance of a martensitic phase by changing the temperature of a Cu-Zn alloy. It was not until the early 1960s that William Beuhler and his colleagues at the U.S. Naval

Ordnance Laboratory discovered the Shape Memory Alloy (SMA) effect in an alloy of nickel (Ni) and titanium (Ti). The team named this alloy "Nitinol (Nickel- Titanium Naval Ordnance Laboratory)" [11]. Although many alloys have been found to exhibit SME, only CuZnAl and NiTi alloys are presently of commercial importance due to the fact that the constituent elements of other alloys are expensive and ill-suited unless they are in the form of single crystals [12]. Furthermore, NiTi alloy was relatively inexpensive and much safer than previous SMAs.

a. Shape Memory Effect

SMAs, also known as "smart material," respond to the changes in temperature and mechanical stresses. They exhibit the SME, which can be described as the effect of restoring the original shape of a plastically deformed sample upon heating to a critical temperature. This phenomenon results from a thermoelastic martensitic transformation. Martensite exists at a lower temperature, which can be deformed easily into any shape by de-twinning. When heated above the transformation temperature, it changes into austenite, recovering to its original shape, as depicted in Figure 3.

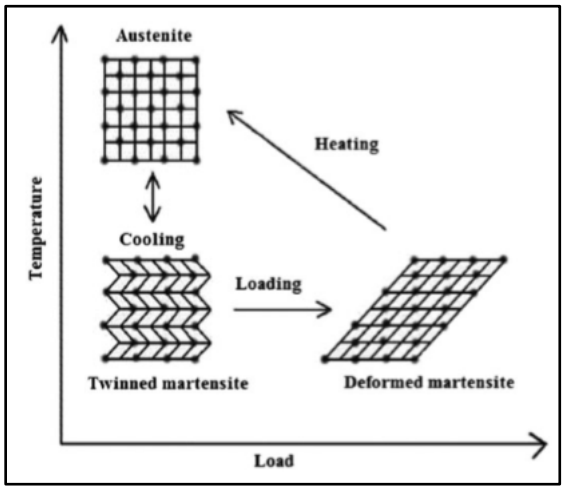

Figure 3. Superelasticity Process. Source: [13].

This cycle may be repeated numerous times as long as the crystalline structure is undamaged. Figure 4 demonstrates the shape memory effect of an SMA wire. The SMA with higher performances can tolerate up to 8% deformation.

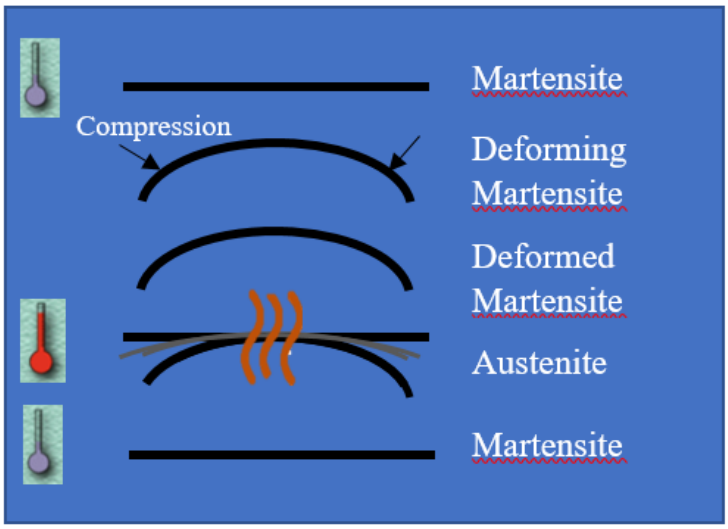

Figure 4. Demonstration of the Shape Memory Effect

b. Nickel-Titanium Shape Memory Alloys

Today, Nitinol is a well-known SMA due to its low cost and excellent performances for various applications. A pure stoichiometric Nitinol is 1:1 atomic ratio consisting of 50–50at% NiTi (or 55–45wt% NiTi). This NiTi intermetallic compound was designated as 55-Nitinol after the discovery at U.S. Naval Ordnance Laboratory [14]. In concurrence with this composition of NiTi alloys, Otsuka and Ren also confirmed that the 50–50at% Ni-Ti is the most reliable composition to exhibit SME [15]. The sintering temperatures from 750 to 1110°F were typically used to preset an original shape; however, the plastic deformation capacity of the alloy and its ability to change back to its original shape when reheated, governed by the temperature at which it was sintered [14]. There is currently no specific sintering temperature that was established to be most effective, as there remains a wide range of temperatures that are being studied to produce NiTi alloys through various fabrication techniques.

c. Phase Diagram

The diverse phases in thermodynamic equilibrium that Ni and Ti can form as well as their solubility and stability of different temperatures and compositions are illustrated in Figure 5. This phase diagram is crucial to understand what heat treatments are needed to stabilize particular chemical compositions. The Ni-Ti phase diagram has evolved over the last 30 years. In particular, the NiTi phase, subject of this study, has been given different temperatures and solubility limits: Laves and Wallbaum initially discovered the presence of a single phase NiTi near the equi-atomic composition at higher temperatures [15], however Margolin et al. and Purdy and Parr discovered that NiTi phase can exist at lower temperatures; however, when lowering the temperatures the range of NiTi solubility also decreases causing the NiTi phase to extend towards Ni-rich portion. Thus, far, the following conclusions have been established by various investigators: (1) The Ti-rich side of the NiTi phase exists when closer to the vertical boundary; (2) The Ni-rich side of the NiTi phase decreases with significant decrease in temperature, and at about 500°C the solubility is insignificant; and (3) The likelihood of eutectoid decomposition at 630°C is unlikely due to the fact that there is no direct evidence obtained [15]. The presence of multiple phases such as Ti_2Ni and $TiNi_3$ at 800°C was reported by Duwez and Taylor [16].

The equilibrium phase diagram suggests that the NiTi phase exists in the central portion of the phase diagram, which is bounded by Ti_2Ni and $TiNi_3$. Within the NiTi phase it can exhibit shape memory behavior between 630 to 1310°C. The composition of Ni-Ti elements also influences the transformation behavior of SMAs. Depending on the heating conditions (temperature and time), the composition can exhibit phases such as Ni_4Ti_3, Ni_3Ti and Ni_3Ti_2.

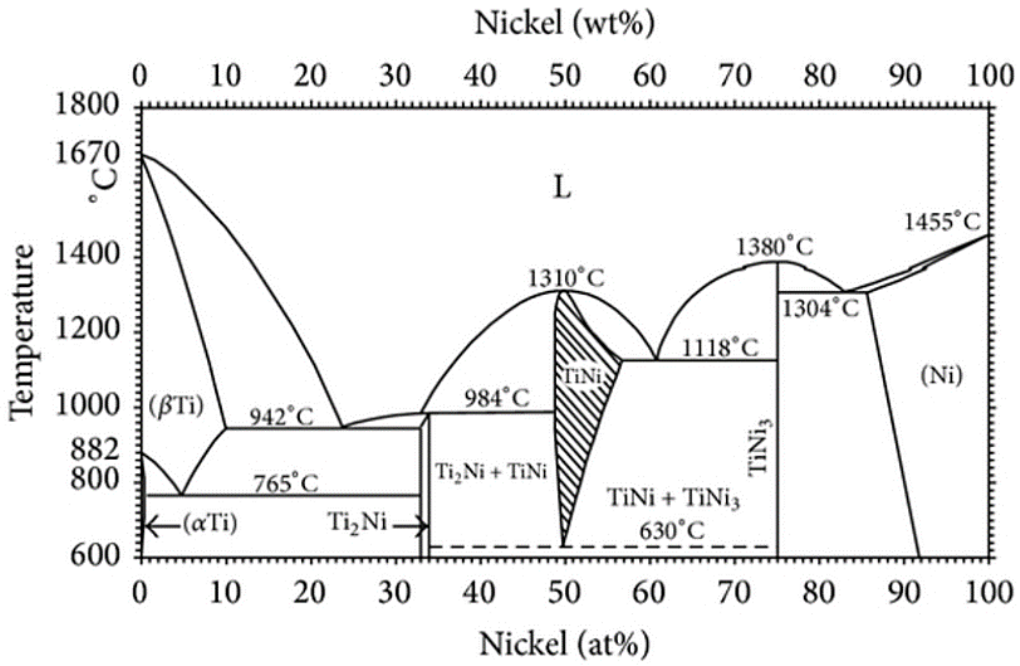

Figure 5. NiTi Phase Diagram. Source: [17].

2. Fabrication Routes for NiTi Alloys

As previously discussed, casting and PM routes can be used to manufacture metals, as well as alloys such as NiTi. The casting process can easily introduce contamination or segregation due to melting and environmental reaction. This process also requires precise composition of Ni and Ti, which can alter the mechanical properties and transition temperature for NiTi. Hence, these factors significantly limit the desire of NiTi alloys production through casting. More commonly used technique in manufacturing NiTi alloys is the PM. In this process, Ni and Ti powder is subjected to sintering to compress the metal powder in binary NiTi.

Table 1 compares and contrasts different NiTi manufacturing methods considering various factors. Due to the high cost of AM equipment, this study focused on providing a proof-of-concept that NiTi alloys could be produced from pastes that included Ni and Ti powders and more affordable approaches to create the green parts followed by conventional sintering (CS) and hot isostatic pressing (HIP).

Table 1. Comparison of Different NiTi Manufacturing Methods. Adapted from [7].

Manufacturing Methods	**Classifications**	**Quality of Product (in terms of surface finish and dimensional accuracy)**	**Defects**	**Porosity**	**Post-processing required**	**Cost**
Casting	VAR	Average	Average (C and O_2, segregation)	35	Machining	Low
	VIM	Average	Average (C and O_2, segregation)	40	Machining	Low
Powder metallurgy	Conventional sintering	Low	High (mixing and sintering defects)	40	Surface treatment	High
	SHS	High	Average (micro-structure control)	65	Surface treatment	High
	HIP	High	Average (decrease internal micro-porosity)	50	Surface treatment	High
	MIM	High	Average (larger parts difficult to fill in furnace)	41	Surface treatment	High
	SPS	High	High (complex parts cannot be fabricated)	12	Surface treatment	High
Additive manufacturing	SLM	Very high	Low/minimum	15	Not required	Very High
	SLS	Very high	Low/minimum	79	De-burring	Very High
	LENS	Low	Low/minimum	16	De-burring	Very High
	EBM	High	Low/minimum	70	Not required	Very High

C. OBJECTIVES

The goal of this research was to develop paste formulations to fabricate NiTi alloys and utilize low-cost AM methods, such as modified polymeric printer, to generate 3D parts. Diverse temperature and pressure conditions were employed to treat the samples after 3D printing. This thesis involved the design, fabrication and characterization of generated SMAs using Ni and Ti powders with different sized particles. By fabricating SMAs using affordable AM route and determining what post-processing methods are needed to achieve the desired properties, instead of using metal printers, we could enable applications that are relevant in diverse engineering fields.

In the last decades, the use of shape memory materials in space systems has grown significantly due to their unique characteristics and many advantages in conditions where traditional methods are no longer applicable. The emergence of such alloys can be seen through numerous technologies in micro-mechanisms, actuators, deployed structures and release devices.

The advantages of using shape memory alloy (SMA) actuators cannot be overestimated. In comparison with traditional electric motors, they offer simple designs, more mass and volume savings, avoidance of shock loadings, silent operation, and overall higher reliability. Moreover, SMA offers excellent damping ability for deployable structures, such as drag or solar sails, solar arrays, and antennas, allowing the deployment scheme to occur in a smooth motion [12]. They do not rely on dampers for shock suppression, as commonly required with springs. This can be seen with the Frangibolt actuators in Figure 6, which are non-pyrotechnic or non-explosive device commonly used in space. SMA can also be operated silently, removing the vibration disturbances to other payloads that are typically associated with motor-driven mechanisms. One example of quiet operating mechanism is the cord-cutting module shown in Figure 7. This cutter utilized a SMA wire (exhibiting the SME) in a way that the element does not come into contact with the cord until the cut is initiated. Another excellent example of SMA functionality is the solar sail deployment system using NiTi SMA wires as shown in Figure 8. Based on Costanza and Tata's experiment, they employed Kapton film with thin

aluminum coating on the surface of the sail. The SMA wires were fastened onto the aluminum surface by high-temperature silicone [18]. By utilizing SMA elements in the deployment design, it has provided greater mobility due to its capability to rotate around the axis. It also reduces the complexity of the deployment mechanism and the weight of the system, particularly for large surfaces. All of these benefits have attracted designers to turn towards SMA as a multifunctional material.

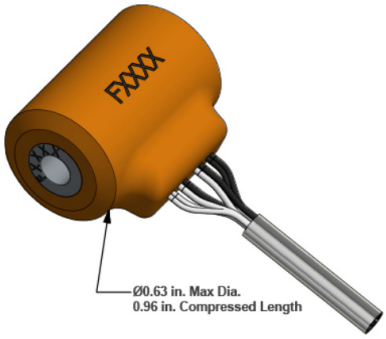

Figure 6. Frangibolt Actuator. Source: [19].

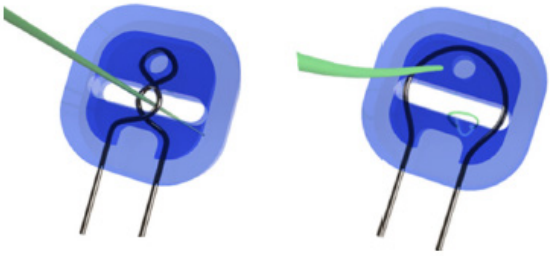

Figure 7. Cord-Cutting Module Using SMA Wire. Source: [20].

Figure 8. Opening Sequence of the Solar Sail Using SMAs.
Source: [18].

The choice of materials utilized in AM remains a key limitation to higher advanced systems. Thus, the integration of small powder materials with AM offers the potential to expand AM technology, as well as complementing existing techniques by modifying the fundamental materials properties [21].

The hypothesis in this research was that it is possible to develop a fabrication route which incorporates particles pastes and a low cost 3D printer to generate SMAs. A positive outcome holds promise regarding cost effective means to fabricate metals and alloys. For instance, when printing onboard a spacecraft or an aircraft carrier, where weight and space are limited, we expect this new fabrication approach to make SMAs more accessible and cost efficient to produce.

Chapter I provides an introduction of this research and background information on SMAs. Chapter II focuses on the experimental methods used for materials fabrication and characterization. Chapter III describes the results found through the different processes that were achieved and the conditions for optimal performance. Finally, Chapter IV leads into the conclusion of this investigation discussing the milestones accomplished, and the future works for further studies.

II. EXPERIMENTAL METHODS

This chapter discusses the procedures utilized to fabricate 3D printed metal structures from NiTi pastes. We started by selecting a binding agent that could either be burned off or evaporated without leaving residues, followed by choosing particle sizes and determining best conditions to 3D print. These steps were followed by deciding the temperatures and environments to sinter them. This chapter also introduces the various methods used for materials characterization. As seen in Figure 9, the experimental procedures have been divided into two main sections to include the fabrication process and the materials characterization.

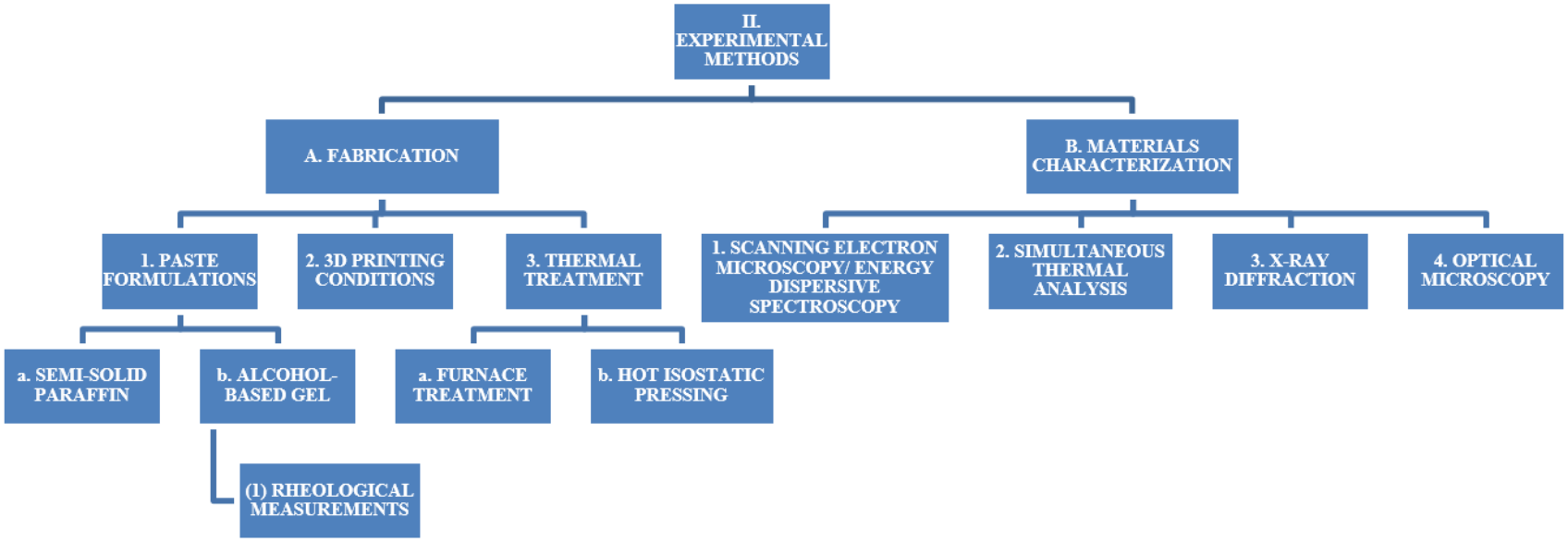

Figure 9. Flowchart of Experimental Approach

A. FABRICATION

1. Paste Formulations

Before developing in-house formulations, we tested commercially available filler infused polylactic acid (PLA) to determine if burning off the polymer will render a sintered metal filler. The tensile strengths of the samples were obtained using the Instron 4507 Tensile Tester in Figure 10.

We initially employed iron, steel, copper and CNT infused PLA produced by ProtoPlant Inc. to print 3D parts. Given our findings presented in Chapter III Section A.1, we decided that there was a need to develop alternatives that will produce mechanically robust metal parts.

Figure 10. Tensile Testing System

The first step in developing the paste formulations was to determine which binding agents or liquid carriers were to be used to integrate with metal particulates. The candidates should have adequate viscosity to be delivered as a paste and should leave no residues upon heating. The metal powders used in this research were: Ni micron powder (5 μm), Ni nanopowder (<100 nm), and Ti (45 μm) in the gel-based formulation while Ti6Al4V (Ti-64) used in the paraffin formulation. These powders were supplied by Sigma-Aldrich

Company located in St. Louis, Missouri. The two binding agents studied were i) a semi-solid, saturated hydrocarbon paraffin and ii) an alcohol-based gel. Both products were available commercially off-the-shelf (COTS).

To prepare the paste, Ni and Ti powders were measured using the analytical balance (Ohaus EP214C Pro). The powders were then combined with the binding agent in a polypropylene (PP) cup, creating a mixture which was stirred at room temperature by hand for approximately one minute, and then transferred to a FlackTek Speedmixer (DAC150.1 FVZ-K), presented in Figure 11, for additional one minute at 300 rpm.

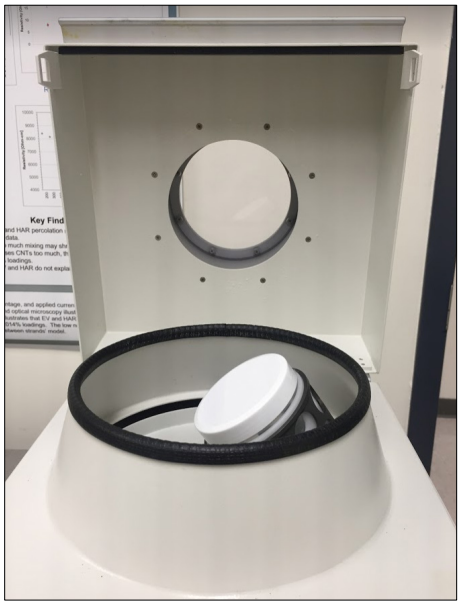

Figure 11. FlackTek SpeedMixer

a. Semi-solid, Saturated Hydrocarbon Paraffin

The first binding agent explored was the semi-solid, saturated hydrocarbon paraffin, referred as paraffin. This material is colorless and odorless. It can be flammable at high temperature, and has a melting point of 50°C. Its kinematic viscosity is 6.2 mm^2/s at 40°C [22].

b. Alcohol-based Gel

The second binding agent examined was alcohol-based gel, also referred as gel. This gel consists of 29% deionized water, 70% ethanol, 1% thickening agent (carbomer, glycerine and triisopropanolamine) by weight. The gel is transparent, flammable liquid and vapor, and its viscosity is 3,500 to 23,000 mm^2/s at 20℃ [23].

(1) Rheological Measurements

The alcohol-based gel mixtures were further analyzed using a Bohlin C-VOR Shear Rheometer. A rheometer is an instrument used to measure the viscosity and shear stress of the fluid flow. This analysis aims to better understand the fluid flow in response to applied force over time because the viscosity of the fluid can significantly affect the extrusion and printing conditions.

In Table 2, various mixtures containing either gel only, or gel with different amount of Ni/Ti powder were prepared by: 1) Measuring the appropriate weight amount of the substance 2) Mixing the substance by hand. 3) Displacing a droplet of metal suspensions onto the sample holder for rheometer test as shown in Figure 12. The formulated fluids were subjected to rheological analyses over a temperature of 25℃. The shear rate ranged from 0.1 to 1000 s^{-1} with the delay and integration time being 5 seconds and 60 seconds, respectively.

Table 2. Samples Tested in a Rheometer

Sample	Composition
1	1 g. gel + 0.611 g. Ni (5 μm) + 0.50 g. Ti (45 μm)
2	1 g. gel + 0.611 g. Ni (nano) + 0.50 g. Ti (45 μm)
3	Pure gel
4	1 g. gel + 0.611 g. Ni(5 μm)
5	1 g. gel + 0.611 g. Ni (nano)

Figure 12. Droplet of a Mixture on Sample Holder

2. 3D Printing Conditions

To 3D print the commercial PLA infused blends, we utilized the same software tools that will be described for the paste formulations, however, we used 1.75 mm filaments and IIIP Monoprice printer.

In this study, we first obtained a computer-aided design STL file of an American Society of Testing and Materials (ASTM) Tensile Specimen E8. This geometry was employed because it is the standard used to test metals and alloys in tension. That is, if successful, the parts produced in this work will be then be tested to determine mechanical characteristics such as yield and tensile strengths, Young's modulus and reduction of area. The STL file was modified using Fusion 360 software [24]. This STL file was then opened and modified in Cura software [25], Figure 13, to incorporate the necessary printing parameters to 3D print the tensile bar. Table 3 lists these printing parameters. The outcome is known as a G-code file, the numerical control programming file used to give instructions to the printer, which enabled the Ultimaker 2+ printer to read the code and initiate the print.

Additionally, the height of the build plate of the printer was adjusted appropriately to ensure the thickness layer was equal in all parts of the print.

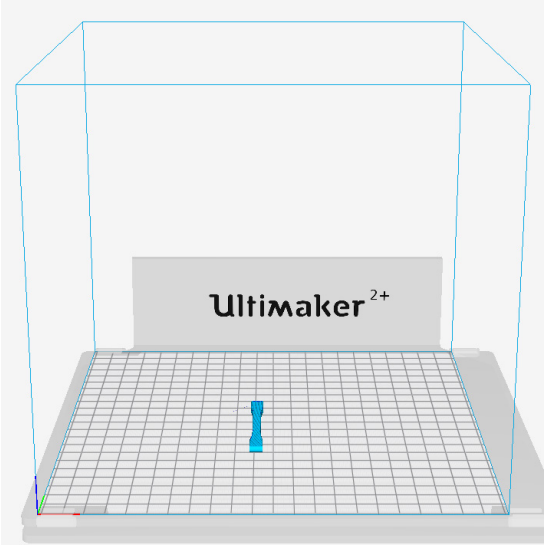

Figure 13. 3D Model of a Tensile Bar

Table 3. Cura Print Setup for Tensile Bar

Layer Height, mm	0.4
Wall Thickness, mm	0.4
Infill Density, %	100
Print Speed, mm/s	20
Travel Speed, mm/s	20
Enable Retraction	Yes

We employed an Ultimaker 2+ printer to which we adapted a syringe pump to deliver the paste. The prepared paste was filled into the syringe. To achieve this, the plastic tubing (4.76 mm) was connected to the tip of the 10 cc syringe while the free end was inserted into the PP cup filled with the prepared paste. The plunger in the syringe was gradually being pulled to fill the plastic tubing and the syringe with the paste. Once the syringe was filled to the maximum, the free end of the plastic tubing was inserted into the 3D printed adapter clip, which was attached to the print head. The male connector was placed at the end of the tubing, and slid up into the recess of the mount. At this point, a chosen PP tip was connected to the male connector as depicted in Figure 14. Various sizes of the nozzle tips, Figure 15, were used depending on the viscosity of the paste formulas generated through numerous trials.

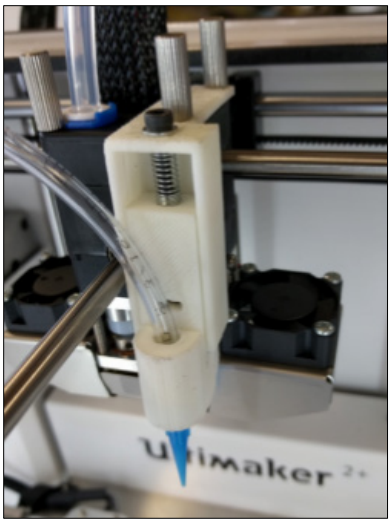

Figure 14. Plastic Tubing Inserted with Nozzle Tip Attached Through an Adaptor Clip

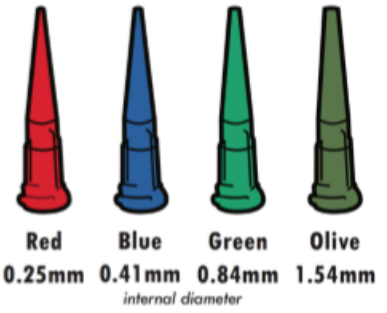

Figure 15. Polypropylene Nozzle Tips

Finally, the filled syringe was positioned onto the extruder motor where the syringe tip pointed towards gravity, illustrated in Figure 16. The positioning of the syringe helped minimize the clogging in the plastic tubing by allowing greater ease of fluid flow due to gravity and force from the motor. When ready to deliver the paste the extruder motor was turned on at the speed between 23.8 to 31.7 cc/hr. At that point, the G-code was selected from the list in the printer, and the printer was initiated. A thin layer of material was deposited onto the build plate to form the outer layer wall and eventually filled the inner

part, which was predefined by the G-code. During the print, the printer fan was also turned on to dry the layers. In total, two layers were printed to form an appropriate thickness of the sample.

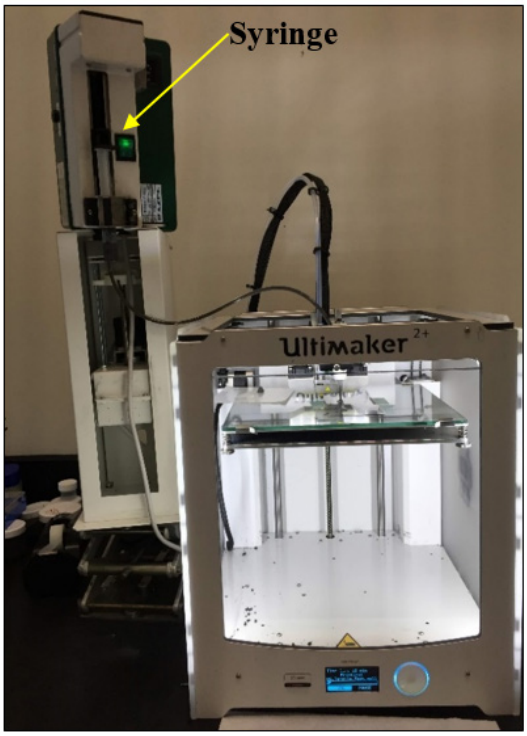

Figure 16. Setup of the 3D Printer

After fabricating 3D printed shapes, all specimens were stored inside the desiccator at room temperature. This allowed the specimens to evaporate and become slightly compacted overnight. The end result was a solid structure composed of agglomerated loose particles that would later be subjected to post-treatment. This part will be referred to as green compact.

3. Thermal Treatment

In this research, CS and HIP were the two primary methods employed for annealing the 3D printed parts. The purpose of this investigation was to evaluate the behaviors and characteristics of the final structures when using different annealing methods at various

conditions. The end goal was to find the most effective method to sinter the particles and produce mechanically robust parts.

a. Furnace

After the 3D printed specimens dried overnight, the next step in fabrication process was to anneal them in order to impart strength and integrity to the overall structure. A Thermo Scientific Lindberg/ Blue-M Furnace (Model TF55035C-1) in Figure 17 was used for heat-treating the green parts. The specimens were annealed under a high temperature and controlled gas environment to avoid oxidation in the sample, depicted in Table 4. To accomplish this, the gas tube was connected to one side of the quartz tube. The opposite side of the quartz tube was then sealed once the sample was placed inside at the center. To purge the system, the gas tank was turned on for about 25 minutes. The gas flow rate for Ar (ultrahigh purity) was set at 91.7 ml/min for purging, and adjusted to 14.9 ml/min when starting the furnace. For N_2 atmosphere, the gas flow rate was set at 121.4 ml/min for purging, and adjusted to 19.8 ml/min when starting the furnace. The system was checked for gas leakage to prevent air from entering the quartz tube.

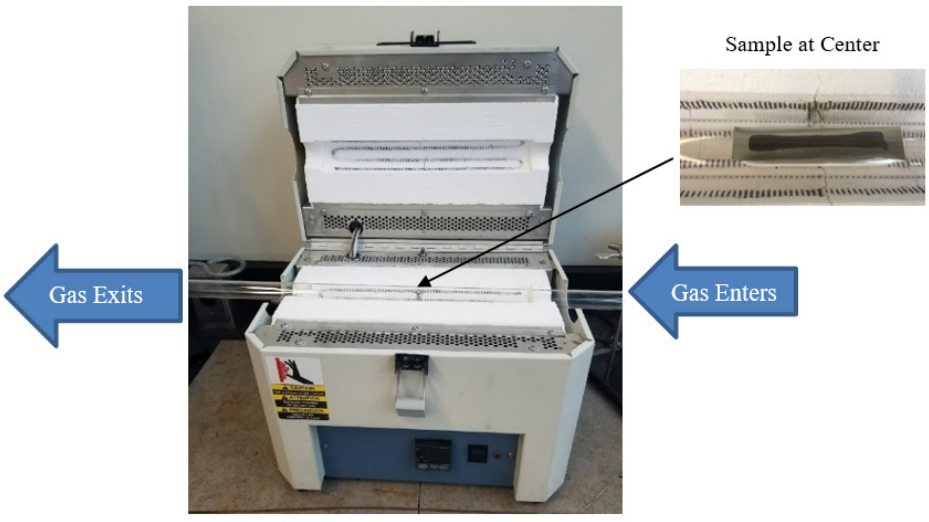

Figure 17. Furnace Setup

Table 4. Different Compositions and Furnace Conditions of Various Samples.

Sample	Gram of Ni (5 µm) powder	Gram of Ni (nano) powder	Gram of Ti (45 µm) powder	Gram of Gel	Sintering Time at 1000℃ (Ar atmosphere)	Ni/Ti- Gel Ratio (wt%)
1	5	0	0	20	1000℃ for 5 hours	20% Ni-80% gel
2	5.03	0	0	7.49	1000℃ for 21 hours	40% Ni-60% gel
3	0	0.25	0.30	1.14	1000℃ for 21 hours	33% NiTi-67% gel

After the furnace tube completed the purge, it was programmed to heat from room temperature (25℃) to predefined 1000°C temperature with the heating rate of 15°C/min. Once, the temperature had reached its maximum it will remain at that temperature for a specified amount of time. After achieving the sintering time, the furnace would eventually cool back down to room temperature and turn off automatically. The gases were manually turned off after the furnace cooled down. As an example, Figure 18 is a plot representing the temperature as a function of time during the sintering process for Sample 1.

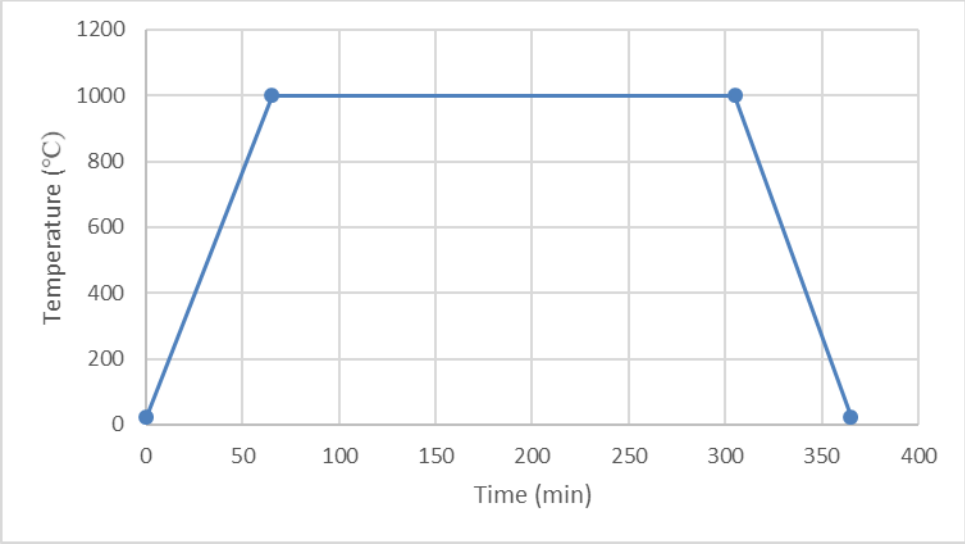

Figure 18. Heating Conditions Plot of Sample 1

b. Hot Isostatic Pressing

The HIP process subjects the green sample at elevated temperature and pressure under a controlled gas atmosphere. HIP service was contracted with American Isostatic Presses, Inc. (AIP), located in Columbus, Ohio. The AIP 6–45H HIP system was used. 3D printed samples composed of specific paste formulations were treated under HIP as listed in Table 5.

Table 5. Different Compositions and HIP Conditions of Various Samples.

Sample	Gram of Ni (5µm) powder	Gram of Ti (45 µm) powder	Gram of CNT	Gram of Gel	Nozzle Tip (mm)	HIP Temperature (Ar atmosphere)	HIP Pressure (MPa)
1	7.66	6	0	14	1.54	1000°C for 3 hours	138
2	7.66	6	0	14	1.54	1000°C for 3 hours	172
3	7.66	6	.07	16	1.19	1000°C for 5 hours	207

Figure 19 represents the plot of the temperature and pressure as a function of time for Sample 1, 2 and 3. The data presented in the plots represent raw data points used during the actual experiment, showing that the pressure ramps are not following a linear profile due to the pressure control.

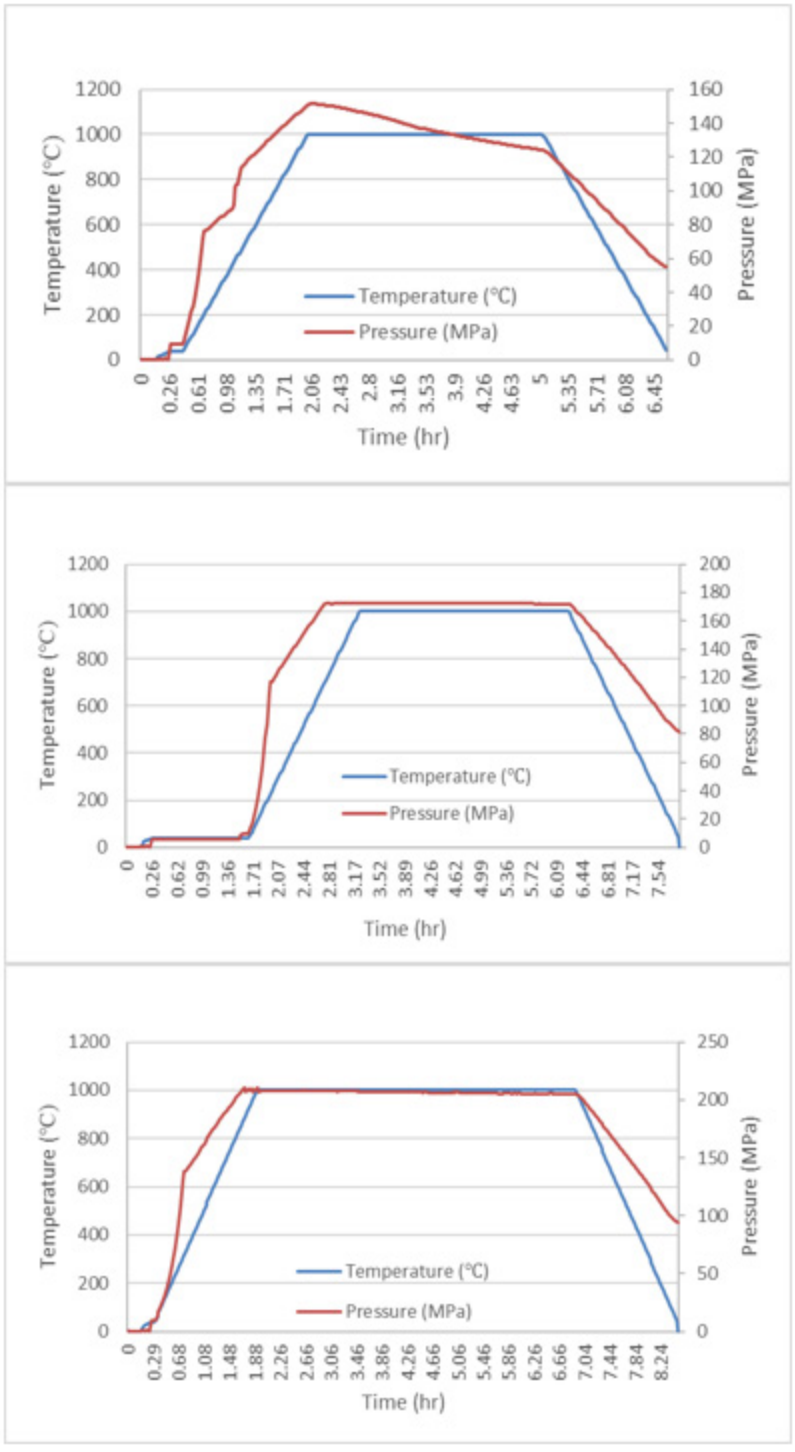

Figure 19. HIP Conditions for Sample 1 (top), Sample 2 (middle), and Sample 3 (bottom)

B. MATERIALS CHARACTERIZATION

To fully understand the behaviors and characteristics of the sintered samples at the microstructure level, multiple characterization techniques were performed. The four primary characterization tools used in this study were SEM-EDS, STA, XRD and optical microscope.

1. Scanning Electron Microscopy/ Energy Dispersive Spectroscopy

Microstructural characteristics such as shapes and sizes of the various samples were examined by scanning electron microscopy (SEM) Ziess Neon 40 FESEM equipped with energy dispersive spectroscopy (EDS) detector in Figure 20. The SEM utilizes electrons as the source focused into a beam to penetrate the surface of the sample. Through the interactions between the striking electrons and the sample, SEM images were generated by collecting the scattered electrons [26].

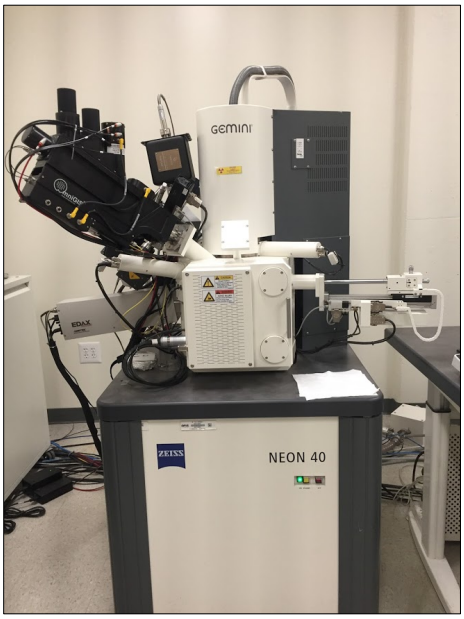

Figure 20. SEM-EDS Instrument

There are various SEM techniques available to produce different images, but the principle type used in this work was: Secondary Electron (SE). For SE, the emitted electron

has energy of less than 50eV. When the high-speed electrons strike the surface of the sample, their kinetic energy gets transferred to the free electrons in the sample. The free electrons with sufficient energy will then escape from the sample by overcoming the strong attractive force of the nuclei. These free electrons are called “secondary electrons,” as depicted in Figure 21.

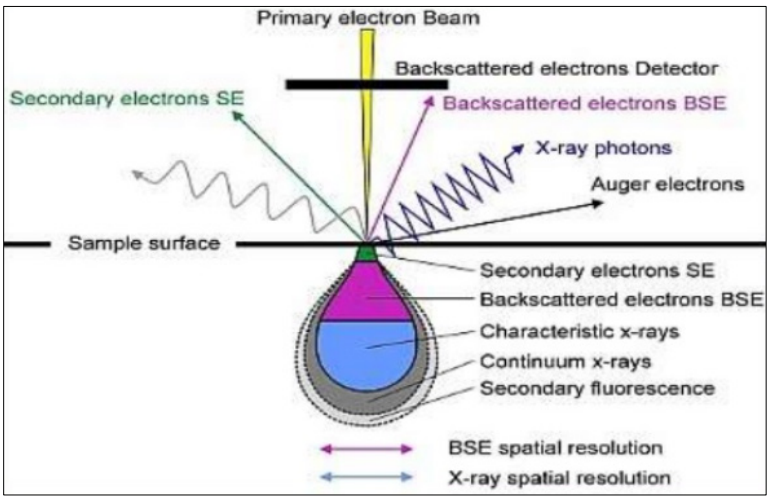

Figure 21. Illustration of Secondary Electron Emission. Source: [27].

EDS systems are integrated into an SEM instrument, so while running the sample in the SEM, EDS was used to scan with EDAX Pegasus Apollo 10 detector to identify the chemical composition, the presence of individual elements and the relative amount of them within the microstructure of the sample. For EDS analysis, the SEM was set to energy of 20keV and current of 1.32×10^{-6} mA.

Using EDS systems, EDS spectrum can be obtained, illustrating a pattern of x-ray counts as a function of energy (in keV). Each energy peak matches the element present in the sample. Samples were prepared by depositing small section of materials onto a carbon tape adhered to an aluminum stub. Samples treated by HIP were mounted in epoxy resin and polished for observation.

2. Simultaneous Thermal Analysis (STA)

The STA (Model: STA 449 F3 Jupiter, see Figure 22) collected both differential scanning calorimetry (DSC) and thermogravimetric (TG) data of the samples under study. This instrument measures changes in samples weight as they are heated and the heat flow of the sample under a well-defined atmosphere. Different properties could be determined from the DSC data including heat capacity, enthalpy of reaction or thermal degradation and enthalpy of melting or fusion [28]. We employed this technique to determine the reactivity of the samples under argon and air atmospheres (TG) and to collect the heat flow signal (DSC) to corroborate the SMA effect. A small quantity of specimens (8-15mg) was placed into sintered alumina crucible, which was inserted into the system.

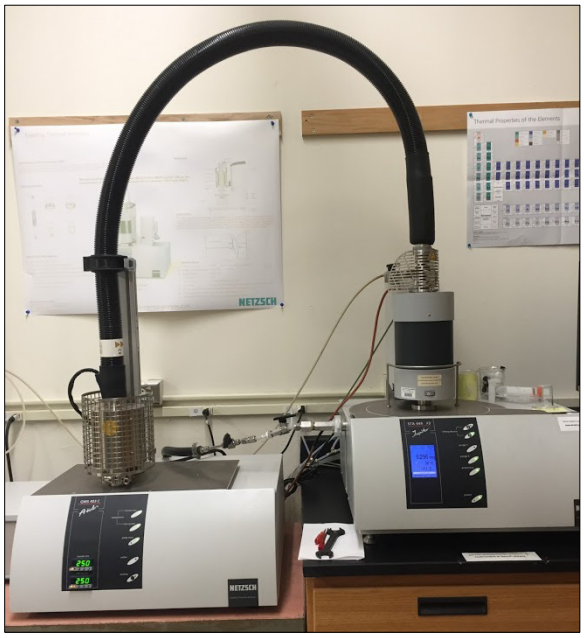

Figure 22. DSC/TG Instruments

3. X-ray Diffraction

Some of the furnace samples were further characterized for X-ray Diffraction (XRD) analysis using a Rigaku Miniflex 600 X-ray Diffractometer shown in Figure 23. This instrument can identify crystalline structures and provides information on lattice constants and geometry, identification of unknown materials, orientation of single crystals,

and defect stresses [26]. For the purpose of this research, the primary use of this tool is to evaluate if the sample suffered any changes during the thermal treatment such as oxidation and nitriding.

Figure 23. X-ray Diffractometer

XRD functions by emitting a collimated beam of X-rays onto a specimen, which gets diffracted by the crystalline phases in the specimen based on Bragg's Law [26]:

$$\lambda = 2d\ sin\theta$$

where λ is the wavelength of the X-ray, d is the spacing between atomic planes, and θ represents the diffraction angle. The information obtained on the diffraction pattern helps identifying the crystalline phases of the specimen and measuring its structural properties [26].

XRD is commonly used in materials characterization because the sample preparation can easily be conducted. The process of preparing the sample consisted of grinding a small piece of sample into fine powder, loading and compacting the sample powder into the sample holder, and mounting the sample holder in the XRD (depicted in

Figure 24). After the analysis, all samples were removed and stored for further characterizations.

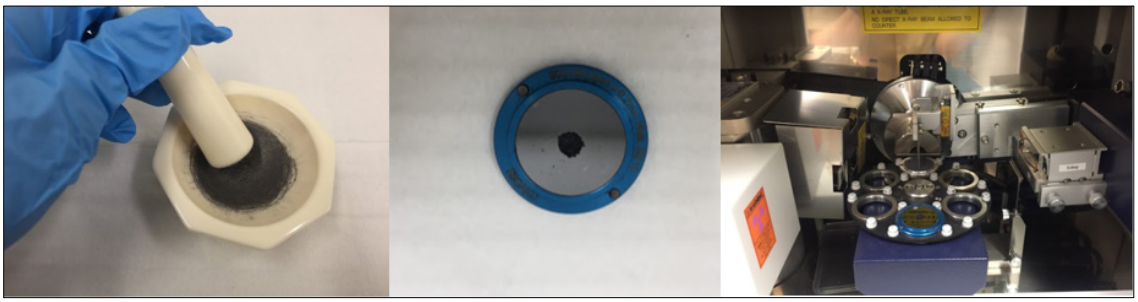

Figure 24. XRD Sample Preparation Process

4. Optical Microscopy

HIP samples were observed and analyzed using the optical microscopy (Nikon Model Epiphot 200), to study mainly the porosity of the HIPped samples. In optical microscope, visible light from the microscope lamp gets passed through the condenser and through the specimen. The condenser is the lens systems that focuses the light from the source onto a tiny spot on the specimen, magnifying images of small specimen. This optical microscope also has a camera that can display the resulting image directly on a computer screen without the need for eyepieces.

III. RESULTS

This chapter presents: the characterization of the metal powders employed, the thermal behavior of the various binding agents, the rheometry of the paste and the analysis of the diverse thermal treatment byproducts. The significance of 3DP process post-treatments using high temperature and pressure will also be discussed throughout the chapter as many experiments were conducted using different conditions. The last section of the chapter includes a discussion section that compares and contrasts the results generated herein for the 3D printed NiTi parts using paste precursors with those published by other authors. The diagram in Figure 25 illustrates the different sections.

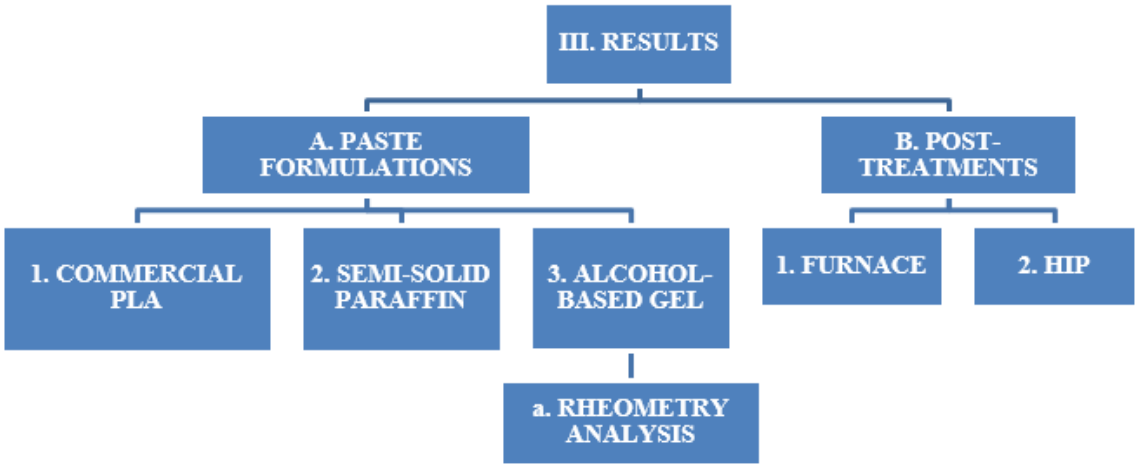

Figure 25. Results and Discussions Layout

A. PASTE FORMULATIONS DEVELOPMENT

As mentioned in the previous Chapter, before testing the paste that we proposed to use as raw materials to produce the printed objects, commercial products, such as polymer infused with fillers, were tested.

1. Commercial PLA with Fillers

As of today, none of the available commercial products can effectively fabricate printed metal parts using a simple and inexpensive polymeric printer. Commercial polymeric filaments filled with micron-sized particles (iron, steel, copper stainless steel and carbon) were printed and their mechanical properties tested.

It was discovered that the printed parts made of PLA infused with metal particulates had extremely low tensile strengths when compared to the standard PLA, as presented in Figure 26. All the filler-containing samples presented lower tensile strengths (TS) than bare PLA, which exhibited TS close to 40 MPa. In contrast, the infused samples of PLA with iron, steel and carbon reached TS of approximately 25 MPa. The specimen infused with Cu particulates exhibited the lowest tensile strength of the group, close to 2 MPa. Based on these results, we determined that PLA infused with metal particulates was not an effective product to generate parts that require mechanical robustness. Although, since the attempt was to determine if the polymeric component could be burned off to produce a metal/alloy, we proceed to perform heat treatments on those samples.

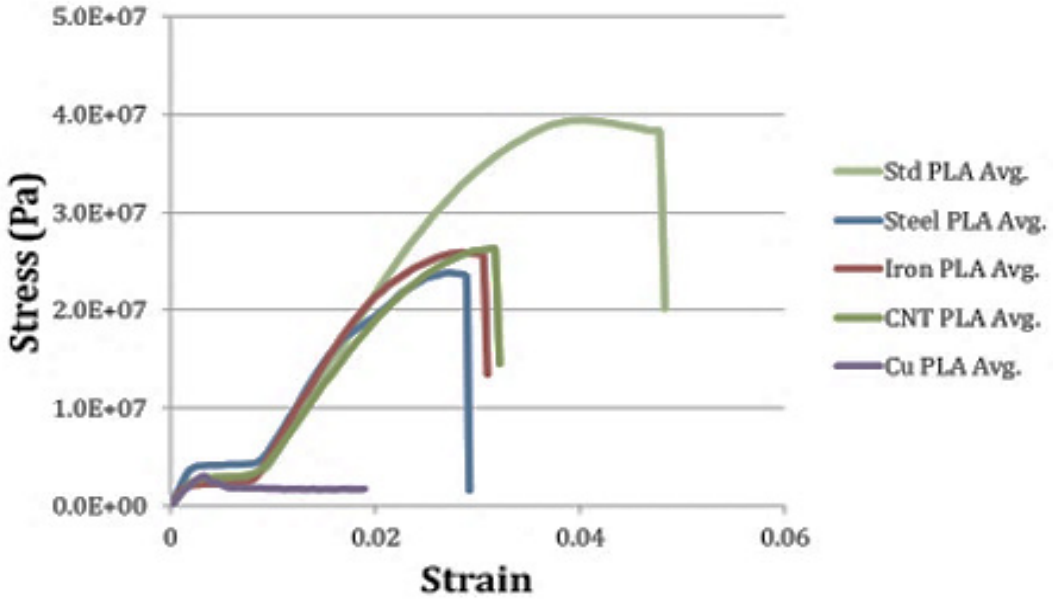

Figure 26. Results from Tensile Tests

The sample infused with copper is presented as an example of such data. Attempts to burn off the polymer using air or oxygen atmospheres at low temperatures (those required to turn the organic components into CO_2 and water, between 200–400°C), followed by higher temperature treatments (600-1200°C) in argon atmosphere, rendered partially oxidized metal particulates, as shown in Figure 27. In the figure, the external layer of the metal particles oxidized despite the change in atmospheres at high temperatures, thus, preventing sintering. Diverse temperature profiles with initial oxidizing atmospheres that were then changed to inert or reducing atmospheres were tested. None of those produced a completely reduced metal/alloy.

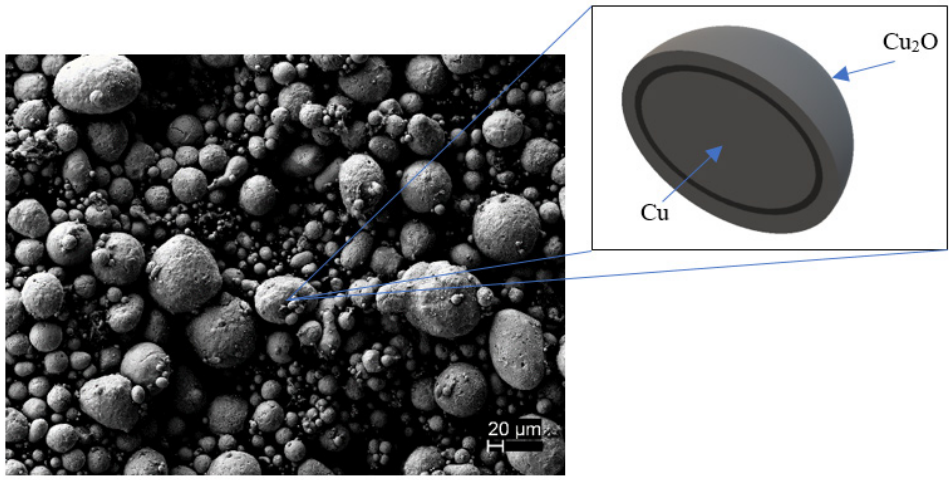

Figure 27. Microscopy Images of the Copper-PLA After Post-Treatment

Burning off the polymer to leave behind only the filler is extremely challenging because it has the tendency to oxidize the particles or to leave carbon behind. The carbon was found in specimens treated in only inert or reducing atmospheres, as marked in the area by the red arrows in Figure 28. These carbon impurities can affect the physical and mechanical properties of the sample, so in this case the use of PLA as the binding agent was unsuccessful because it did not evaporate cleanly, leaving contaminations on the specimen.

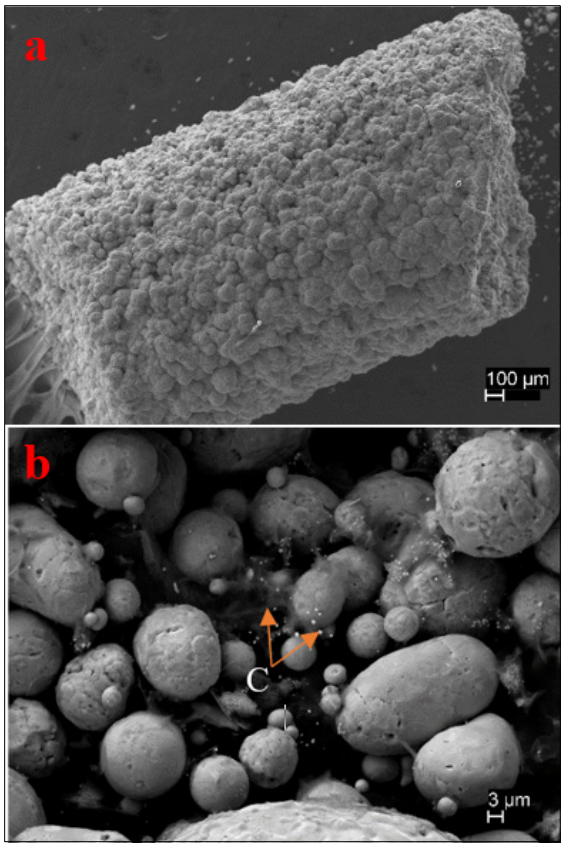

Figure 28. Microscopy Images of (a) Copper part that oxidized produced from a PLA-Cu filament and (b) Carbon residue observed in a PLA-Cu filament sample that was annealed using inert atmosphere

By evaluating and understanding the previous work conducted, it opened the door to the next chapter of other possibilities. The next challenge was to find suitable binding agent that could be removed without modifying composition of the sample, and yet exhibited the appropriate viscosity for 3DP.

Various paste formulations were developed using different binding agents, Ni and Ti powders. The Ti (45 µm) and Ni (nano and 5 µm) powders were about spherical in shape as depicted in Figure 29. The SEM images (top to bottom) show that the sizes of the Ti (45 µm) particles ranged from approximately 15 to 60 µm with few smaller outliers; the Ni (nano) particles were from 10 to 200 nm with a mean value of 100 nm; and the Ni (5 µm) particles were between 1 to 15 µm with a mean value of 6 µm.

The results from the fabrication and characterization processes enabled us to determine which binding agent was most adequate to be utilized in the paste formulations with the end goal that upon thermal treatment will leave only alloy components free of organic solvents.

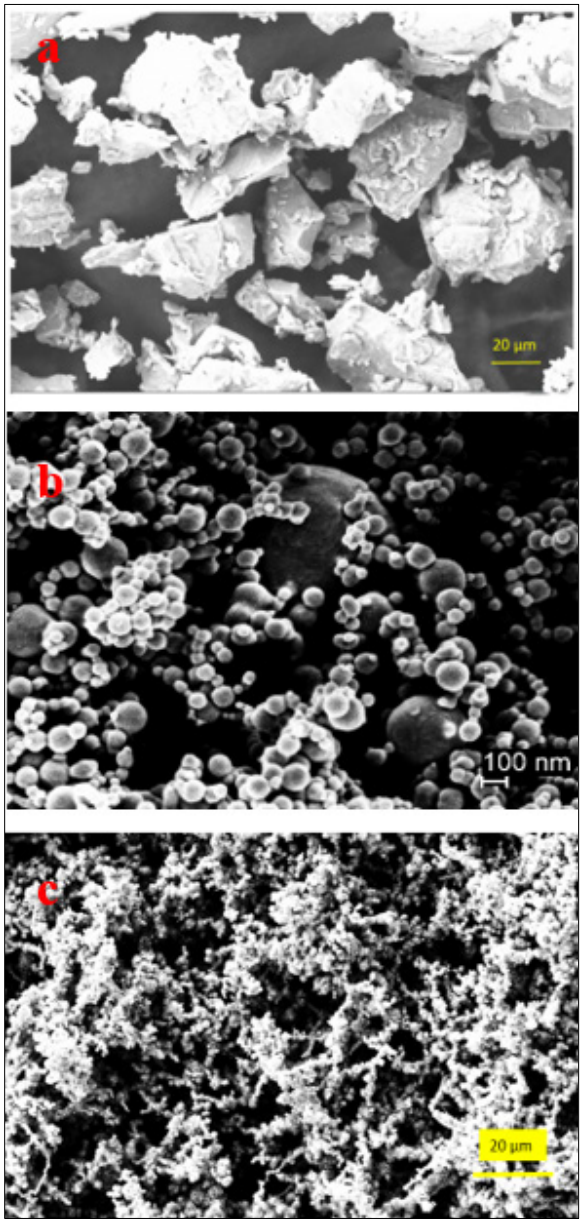

Figure 29. SEM Images of Raw Powders: (a) Ti (45µm), (b) Ni (nano), (c) Ni (5µm)

2. Semi-solid, Saturated Hydrocarbon Paraffin

During the initial study, paraffin was the binding agent used to create a paste with metal particles such as, Ti-6Al-4V or Ti-64 (titanium alloy). Ti-64 powder was mixed with paraffin (1:1.4 ratio) to create a sample that was analyzed by thermogravimetric (TG) in order to determine what byproducts were generated. The first TG measurement was carried out on the specimen using N_2 environment at 550°C for approximately six hours. The second measurement consisted of the same mixture and heating conditions, but the sample was treated in Ar environment.

The results presented in Figure 30 illustrate the TG behavior observed for the two samples with different gas atmospheres. The mass changes of the sample under Ar and the sample in N_2 did not differ significantly, about 1% difference. The analysis showed that the masses of both, Ar and N_2 treated samples stabilized when reaching temperatures of 500°C with total mass losses of 13.04 and 14.29% respectively. The sample in N_2 atmosphere reached stabilization slightly faster than the sample in Ar.

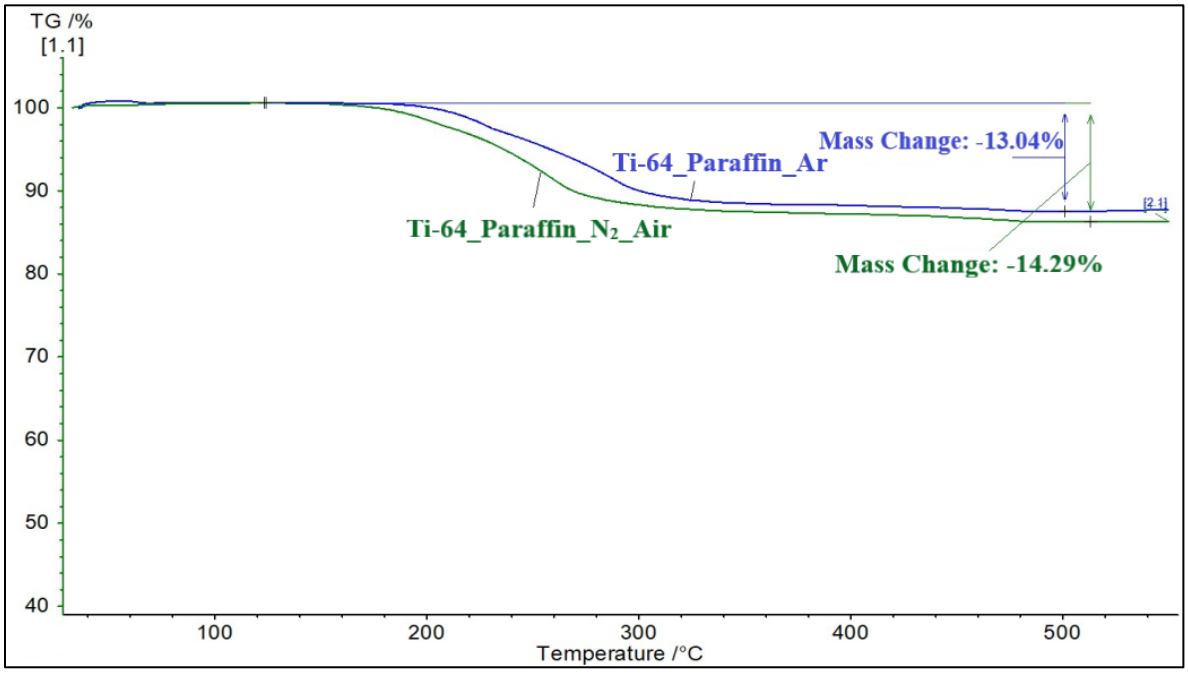

Figure 30. TG Comparison of Samples in Different Gas Atmosphere

In addition, the residues were subjected to SEM analysis to determine their microstructural characteristics. Based on the SEM image and EDS analysis shown in Figure 31, Ti-64_Paraffin_N_2 sample contained nitrogen, mostly in the surface of the particulate, which could explain why the particles did not sinter together. Titanium nitrides could be formed when cured under nitrogen atmosphere at high temperatures [29]. Also, small amounts of aluminum (Al) and vanadium (V) were present due to the inherent composition of Ti-64 alloy. No other residues of the paraffin-binding agent were observed. In sum, nitrogen atmospheres and high temperatures promote a burn off of a paraffin that produces mainly an alloy. However, the alloy contains traces of TiN, which might change the mechanical properties of the product and should be avoided. It is worth mentioning that a similar composition is found in samples produced by direct metal laser sintering [30], [31].

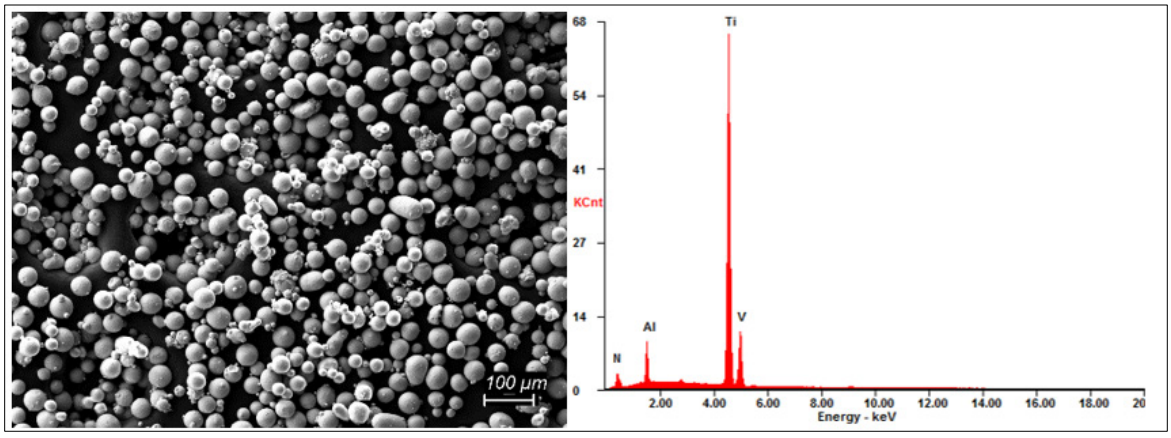

Figure 31. (a) SEM Image and (b) EDS Analysis of Ti-64 and Paraffin Under Nitrogen

In contrast, the sample treated in argon atmosphere (Ti-64_Paraffin_Ar), Figure 32, shows that the particles sintered together. No traces of nitrogen were present in the sample. However, some carbide was introduced in the sample as depicted in the XRD analysis, Figure 33. The XRD peaks correlate with titanium vanadium carbide. The carbide in this sample seems to be a byproduct of the organic paraffin binder decomposition, a similar situation than the one encountered when burning off PLA in the last section. With this in

mind, it is important to note that an abundance of titanium carbide in the sample can significantly compromise the structural integrity and material properties of the metal alloys.

In fact, any presence of carbon, nitrogen or oxygen in the treatment process is highly unwanted because it can formulate titanium nitrides, oxides and carbides. These hard inclusions act as discontinuities, reducing the strength of the metal alloys such that it could lead to device failure.

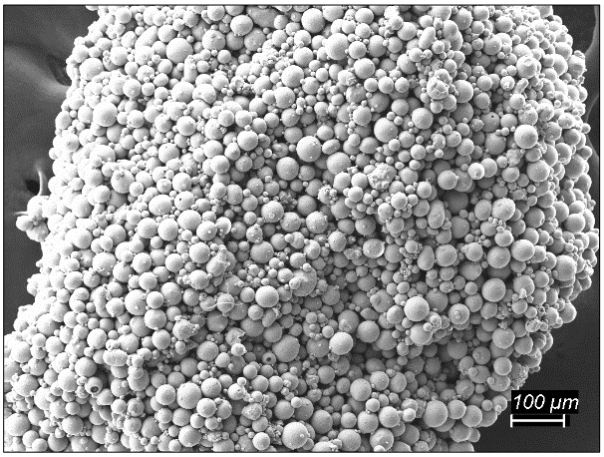

Figure 32. SEM Image of Ti-64 and Paraffin under Argon

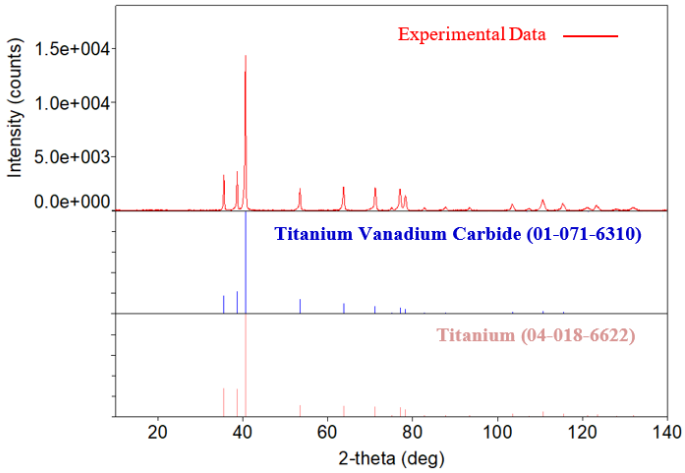

Figure 33. XRD Pattern of Ti-64 sample mixed with paraffin and heat treated to 1000°C using Argon atmosphere

Another issue with using paraffin as the binding agent was its high viscous characteristic. The natural state of paraffin is semi-solid, so this substance can be very thick at room temperature, making it extremely difficult to combine with metal particles uniformly. More importantly, trying to 3D print a part with this substance was extremely challenging because the flow was exceedingly hard to deliver the paste through the plastic tubing. Eventually, the flow would discontinue because not enough force could be applied with an extruder motor to push the remaining paste out of the syringe.

The findings based on visual observations and materials characterizations proved that paraffin exhibits too high of a viscosity to perform effectively in a 3D printer. It also failed to evaporate cleanly when exposed to high temperatures, leaving behind residues such as nitrogen or carbides. In overall, paraffin deemed to be an inadequate choice for the binding agent used in the paste formulations. Hence, another alternative for binding agent was explored.

3. Alcohol-based Gel

An alternative to the paraffin was the alcohol-based gel. To investigate if the gel can evaporate cleanly, a sample was prepared by mixing 1.14g of gel with 0.30g of Ti (45 μm) and 0.25g Ni (nano) powder. This mixture was equivalent to 33% NiTi and 67% gel. A small droplet of this mixture was placed onto the sample holder, left to dry and the residues were analyzed in the XRD, and as seen in Figure 34, only Ni and Ti peaks are present with no other byproducts that presented a crystalline phase.

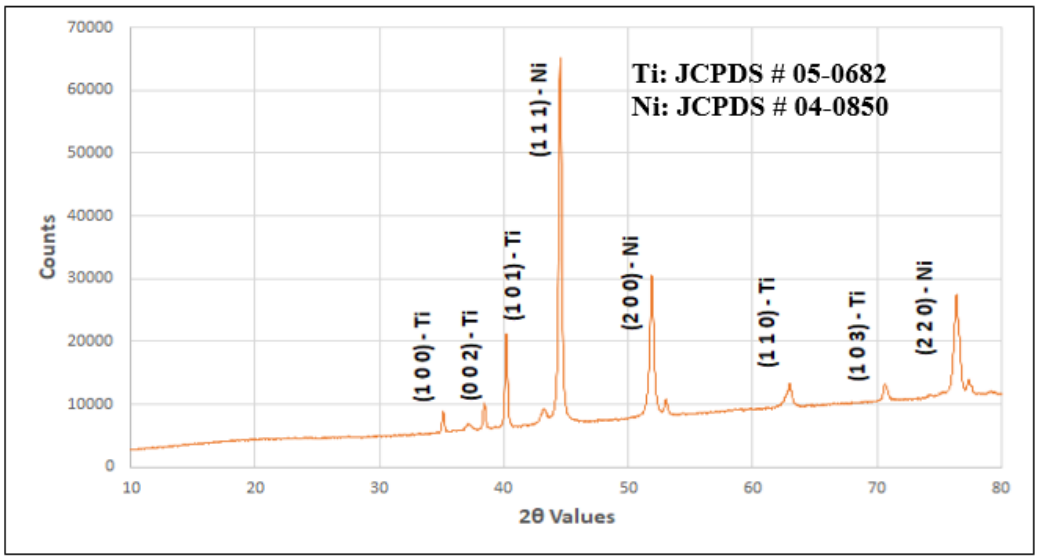

Figure 34. XRD Pattern of Mixed Ti (45 µm) and Ni (nano) Powder with Gel

Not only did the gel evaporated cleanly with no residues, it was successfully delivered in a 3D printer due to its adequate level of viscosity. To illustrate how gel acted as an excellent binding agent when fused with Ni (5 µm) particles, Figure 35 demonstrates a successful trial resulted in a 3D printed part. By combining gel and metal powders together, the consistency of the paste was much more homogeneous and easily delivered in a 3D printer. Consequently, the gel was employed from this point on in many experiments to bind metal particles together.

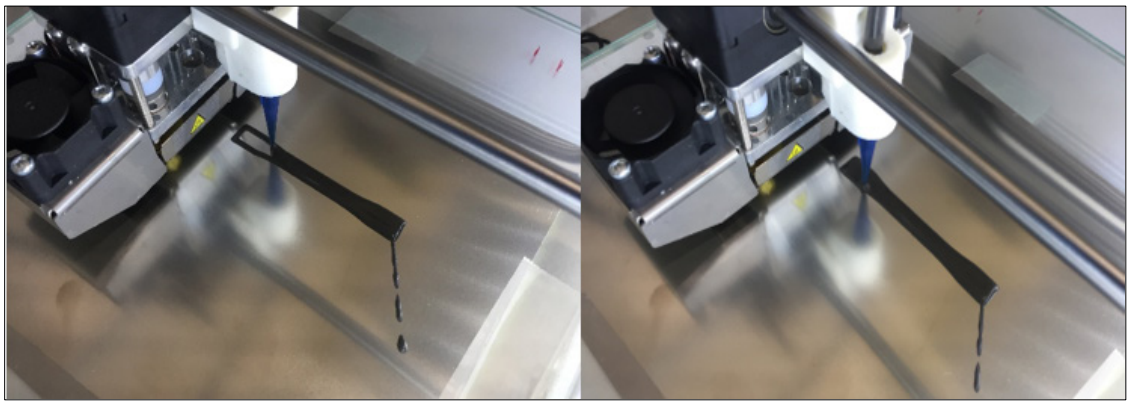

Figure 35. A 3D Printed Part

a. Rheometry Analysis

The viscosity of various pastes was tested using a rheometer. The decision to perform rheometry analysis stemmed from the observations that samples containing Ni nanoparticles separated from the mixtures during the speed mixing operation, as seen in Figure 36. The sample with Ni nanoparticles behaved similarly to a thinning agent, as opposed to the sample containing Ni (micron) particles that successfully provided a paste consistency. Thus, this rheometry test aimed to further investigate the rheological behavior of the fluids containing different metal sized particles. It was also to provide supporting data to verify observations that Ni nanoparticles behave differently than the micron-sized particles. The samples listed in Table 2 from Chapter II, Section A.1.b.1, were tested.

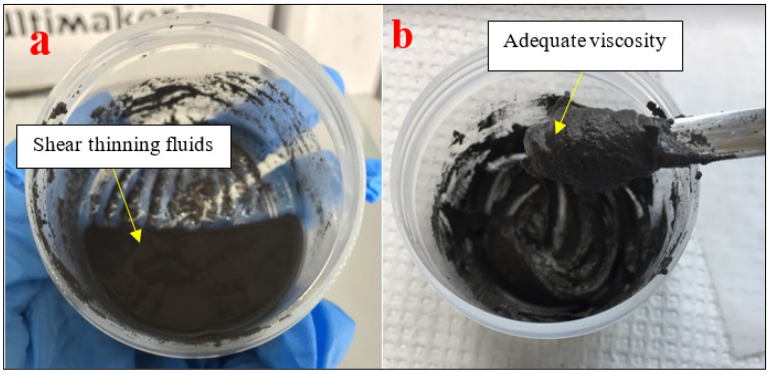

Figure 36. Mixture of Gel with (a) Ni (nano), (b) Ni (5 µm)

The viscosity of samples containing alcohol-based gel, Ni (5 µm) and Ti (45 µm); and alcohol-based gel, Ni (nano) and Ti (45 µm) are presented in Figure 37. Both samples initially show steady decline in the viscosity as the shear rate increases. However, at about shear rate of 19 s^{-1} the viscosity of sample containing Ni nanoparticles rapidly decreased from 10 to 0.005 Pa-s. The changes in the viscosity could also be verified visually in Chapter III, Section B.1.

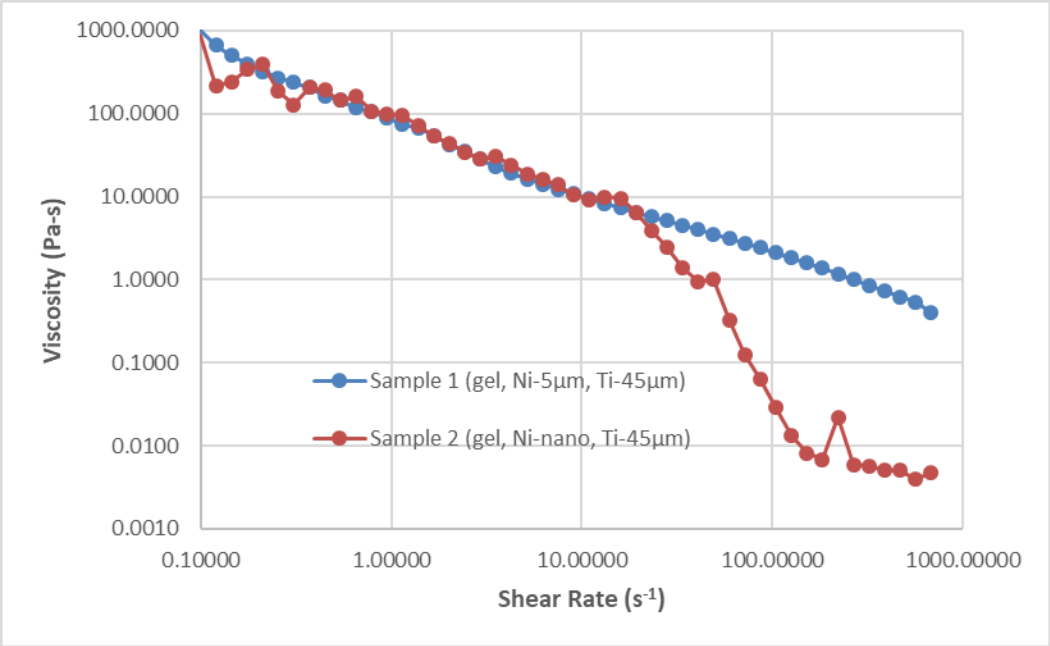

Figure 37. Viscosities of Samples Containing Ti (micron) and Ni (nano and micron) Particles vs. Shear Rate

Figure 38 illustrates the shear stress as a function of the applied shear rate in a logarithmic scale for sample containing the Ti with either Ni nano or micron particles. The sample containing only micron-sized particles shows a positive linear trend in the shear stress as the shear rate increases. This corresponded to a Newtonian fluid behavior. By contrast, the sample containing Ni nanoparticles shows an initial increase in shear stress, but at shear rate of 16 s^{-1} it decayed exponentially. Based on the viscosity and shear stress behaviors of this sample, there was a strong indication that the fluid resembled non-Newtonian. Specifically, this type of fluid is known as pseudoplastic or shear thinning in which the viscosity decreases with increased shear rate. Experimentally, a shear thinning behavior will affect the gel to become more fluid and separate from the particles, which cause clogging of the nozzle.

The compositions of the samples were almost identical with the exception of the particle sizes of Ni powders, so this led us to believe that the differences in particle sizes of Ni powders caused of dissimilar rheological behaviors in the two samples. Therefore, additional rheological measurements were performed in an effort to gather more supporting

evidence to justify why Ni nanoparticles failed to mix adequately with gel to be delivered as a paste.

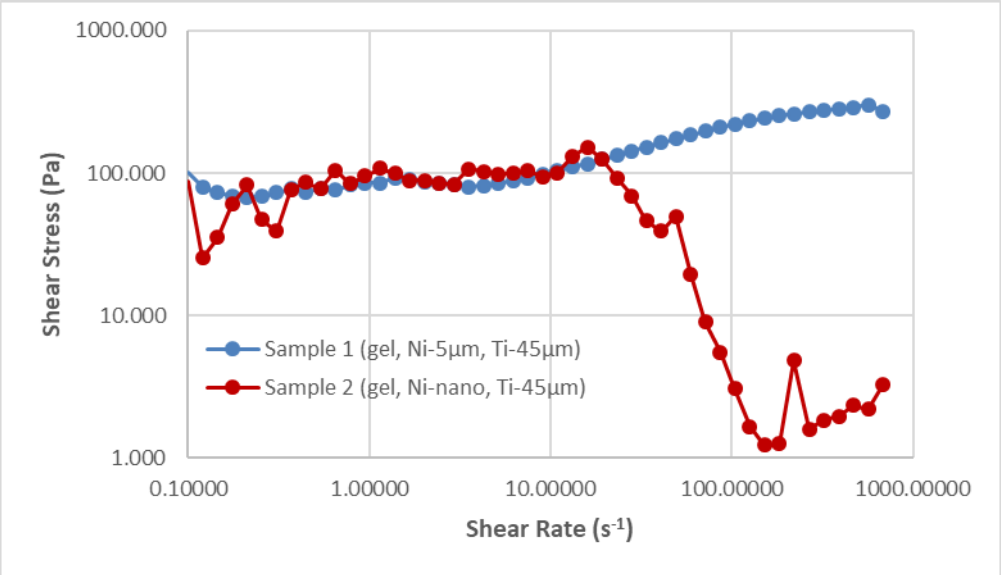

Figure 38. Shear Stress of Samples Containing Ti (micron) and Ni (nano and micron) Particles vs. Shear Rate

Further rheometry analysis was conducted with additional samples composing of: (a) pure gel, (b) gel and Ni-micron, and (c) gel and Ni-nano. In Figure 39, all samples share a commonality in that the viscosity decreases with the increased shear rate. But, the Ni-nano sample shows an apparent decrease in viscosity at approximately 152 s^{-1}. A similar behavior of this sample was seen in Figure 40, illustrating the rapid decline in shear stress occurring at about 152 s^{-1}. The characteristic of Ni-nano sample correlate to an irregular non-linear trend. On the contrary, pure gel and Ni-micron samples indicate either a gradual increase or constant shear stress in a linear trend over increased shear rate. To conclude, the fluid behaviors of Ni-nano sample confirmed that shear thinning exists when introducing Ni nanoparticles into the mixtures.

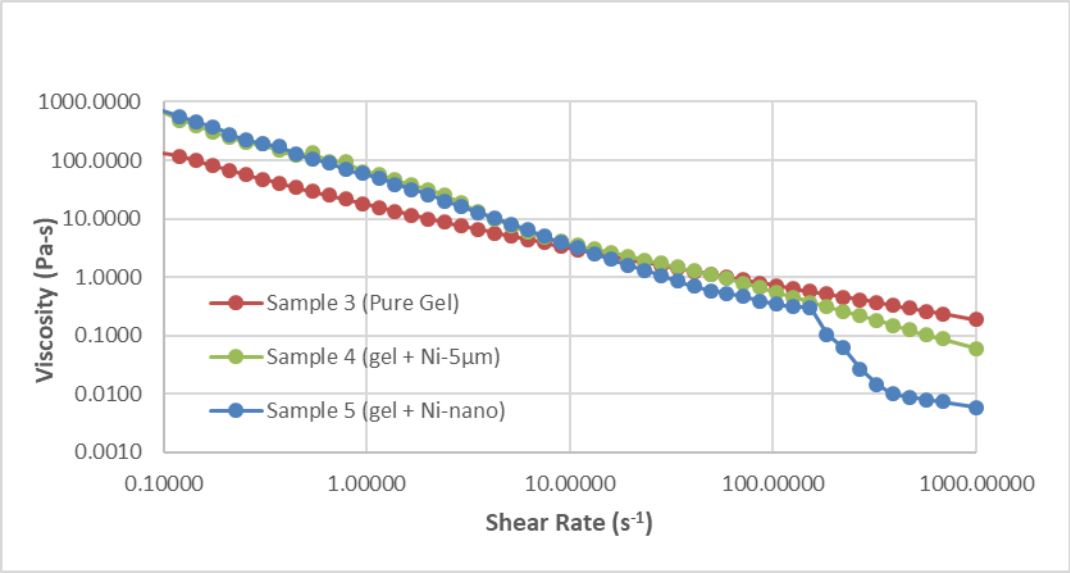

Figure 39. Viscosity of Samples Containing Pure Gel Only or Gel with Ni (nano or micron) vs. Shear Rate

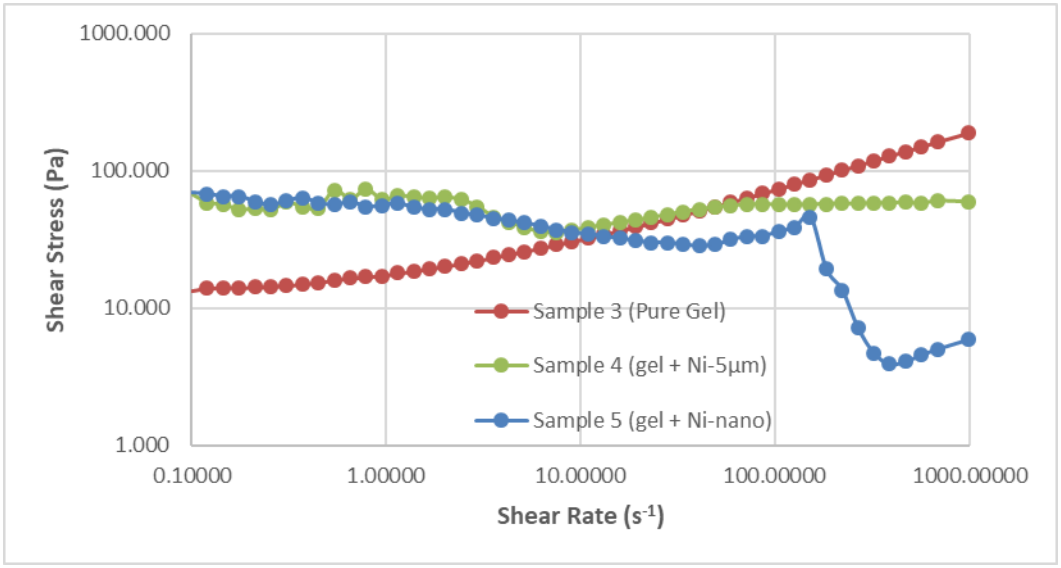

Figure 40. Shear Stress of Samples Containing Pure Gel Only or Gel with Ni (nano or micron) vs. Shear Rate

Tseng and Chen [32] have also examined similar work in the rheology of Ni nanoparticle inks consisting of Ni nanoparticle, terpineol (liquid carrier) and various polymeric surfactants. In their research, they discovered that the concentrated nanoparticle inks exhibited a shear-thinning flow with the increased shear rate regimes and solids-

loading [32]. They suspected that the increase in applied shear force causes the ink network to break down to the point in which the resistance to flow is reduced. This nanofluid behavior could also be correlated to the rheology results of our samples containing Ni nanoparticles.

B. POST-TREATMENTS OF 3D PRINTS

The green compacts require post-treatment to fuse the particles together to produce dense final products. Thus, the CS method was conducted to heat treat the specimens using a furnace. Table 4 (from Chapter II, Section A.3.a) represents the details of each sample's composition and heating conditions in argon environment.

1. Furnace

A sample made up of 20% Ni (5 μm) and 80% gel was 3D printed using a 0.41 mm nozzle tip and was subjected to sintering at 1000℃ for five hours in argon atmosphere. Figure 41 represents the SEM images of this sample after heat treatment in different magnifications. The image shows that the particles were sintered, which is the act of fusing particles together and forming one large cluster. The black areas in between the sintered particles represent the void spaces, porosity. We suspected that the porosity level was affected by the high amount of gel used in this paste formula.

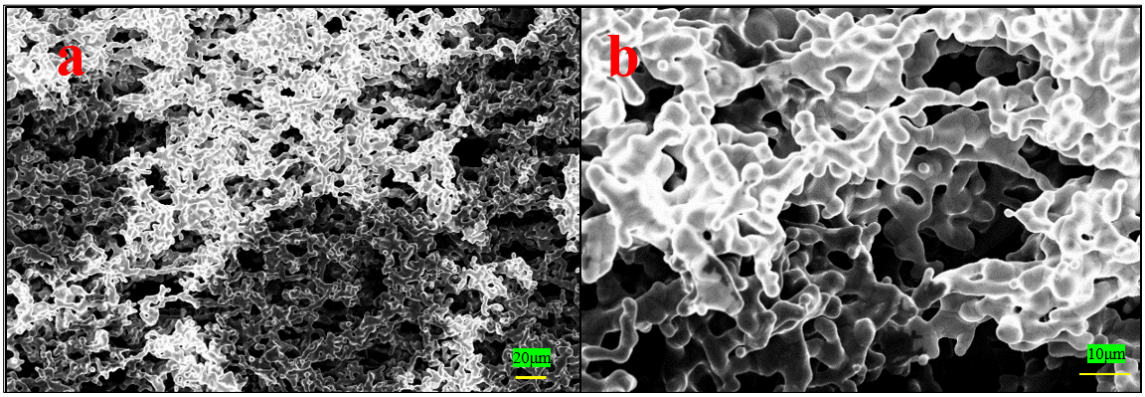

Figure 41. Sample Containing 20% Ni (5 μm) and 80% Gel after Sintering at Magnification of (a) 300x and (b) 1000x

EDS analysis confirms no presence of impurities after the sample was heat treated. Only Ni element was detected in the sample as shown in Figure 42. This initial trial using CS approach proved that thermal treatment in a furnace was effective in sintering the Ni particles together with no byproducts, and that gel could be burned off completely with no residues at 1000℃. However, the porosity level of the sample still remained a challenge because there were various possible factors that could affect the porosity including, the amount of gel used, sintering conditions and 3DP process. The subsequent experiment was reducing the amount of gel used in the paste formulations and prolonging the sintering time from five to 21 hours, in an effort to minimize the pores in the samples.

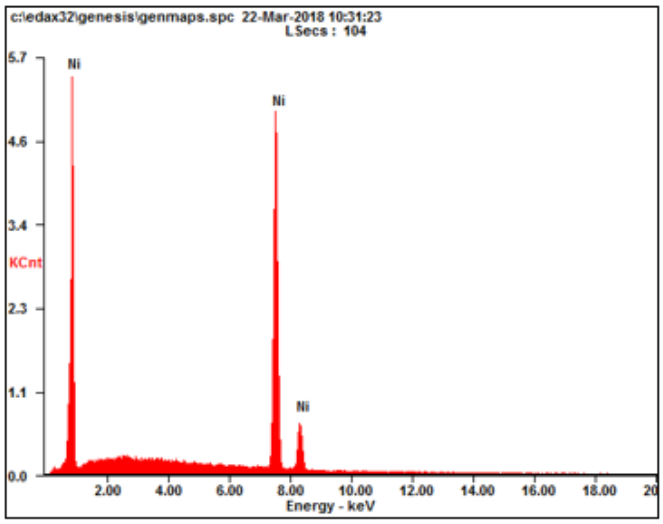

Figure 42. EDS Plot of Sample Containing 20% Ni (5 µm) and 80% Gel After Furnace

A sample containing 40% Ni (5 µm) and 60% gel was 3D printed in the second trial. The SEM image after post-treatment in Figure 43 shows a significant decrease in porosity comparing to the 20–80% Ni/gel sample. EDS analysis also confirms no presence of other impurities, and only Ni element was detected as shown in Figure 44. This trial was a success in proving that the porosity of the treated sample was minimized by reducing the amount of gel and increasing the sintering time.

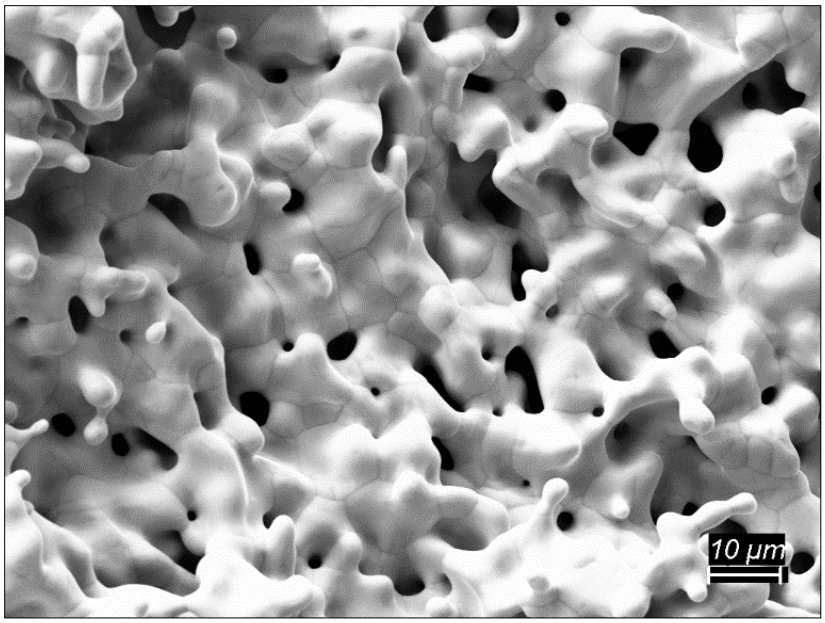

Figure 43. SEM Image of Sample 40% Ni (5 µm) and 60% Gel at Magnification (1000x)

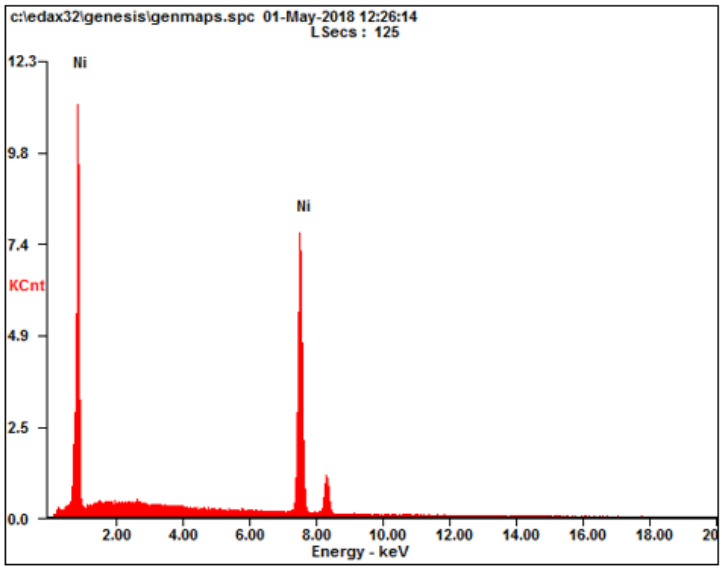

Figure 44. EDS Plot of Sample Containing 40% Ni (5 µm) and 60% Gel after Furnace

To evaluate if reducing the particles size could enhance the sintering mechanisms, we employed Ni nanoparticles in the following sample. A sample, made up of 33%Ni

(nano)-Ti (45 μm) and 67% gel, was subjected to sintering at 1000°C for 21 hours in argon atmosphere. Figure 45 shows the sample prior to and after sintering in the furnace. As seen, the sample after post-treatment shrunk significantly, and failed to retain a near net shape. The color of the treated sample also changed to light gray, suggesting that oxidation might have occurred.

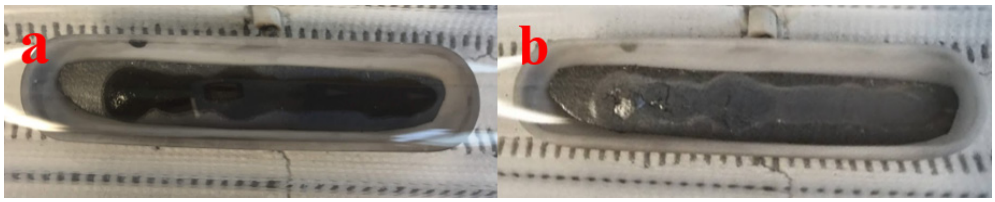

Figure 45. Sample Containing 33% Ni (nano)-Ti (45 μm) and 67% Gel (a) Prior to Sintering and (b) after Sintering

The XRD analysis in Figure 46 indicates that the main peaks correspond to the Ni structures, however, small peaks of titanium oxide (TiO_2) were also present in the sample after post-treatment. The formation of TiO_2 in the sample indicates the presence of oxygen during the sintering process in flowing argon. Wu et al. suggested that the surface oxidation of the alloy could be from the oxygen contamination found in the laboratory grade argon gas [33]. However, in our case, ultrahigh purity argon was used indicating that oxidation occurred from leakage in the furnace system. From this point on, the experiments were conducted carefully to ensure that the system was hermetically sealed.

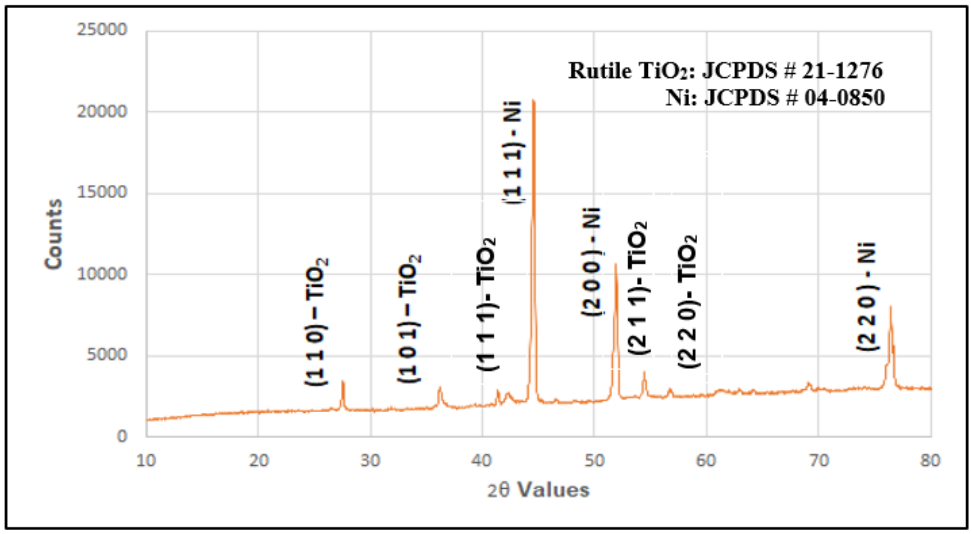

Figure 46. XRD Pattern of Sample Containing 33% Ni (nano)-Ti (45 µm) and 67% Gel After Sintering

In addition to XRD analysis being used to characterize the materials, SEM/EDS was also utilized to identify the sample's compositions and measure the relative amount of individual elements present. The analysis shown in Figure 47 indicates that the sample contained about 41–59% Ni-Ti by weight, relatively different than those represented by typical NiTi shape memory alloys (55-45% Ni-Ti). However, it is important to note these differences in the chemical compositions as it will be discussed subsequently. The SEM image shows that Ni and Ti particles were sintered and the particle sizes ranged from approximately 1 to 50 µm. This sample was compared to commercial Nitinol wire to identify phases and precise compositions.

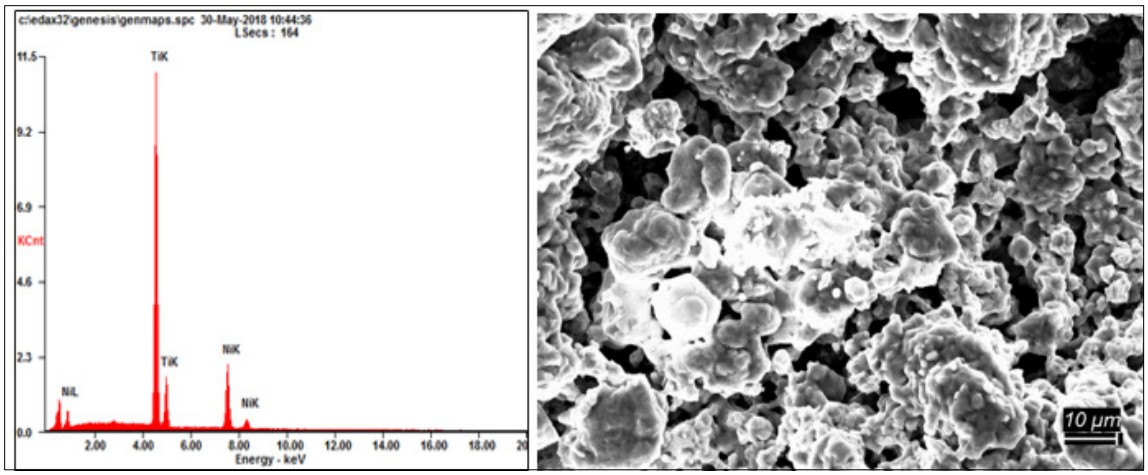

Figure 47. Sample Containing 33% Ni(nano)-Ti (45 µm) and 67% Gel: EDS Plot (left) and SEM Image at 1000x Magnification (right)

The commercial Nitinol sample exhibits porosity and surface defects, as marked in Figure 48. The EDS results in Figure 49 were obtained for the commercial Nitinol. The 39wt% Ti and 61wt% Ni are outside the ideal compositions for shape memory effects based on the phase diagram in Figure 5 (from Chapter I, Section B.1.c). However, the commercial Nitinol still exhibited the shape memory effect.

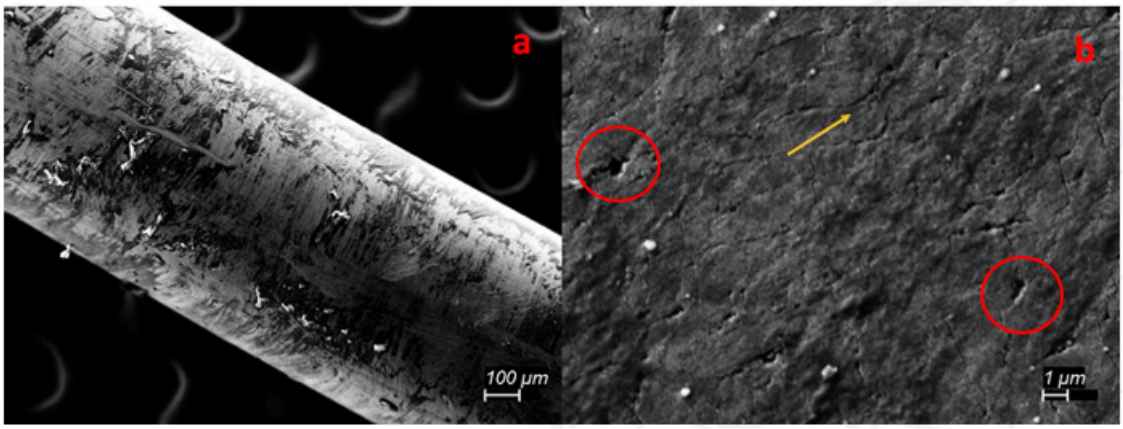

Figure 48. Commercial Nitinol Wire at Magnification of: (a) 70x, (b) 5000x

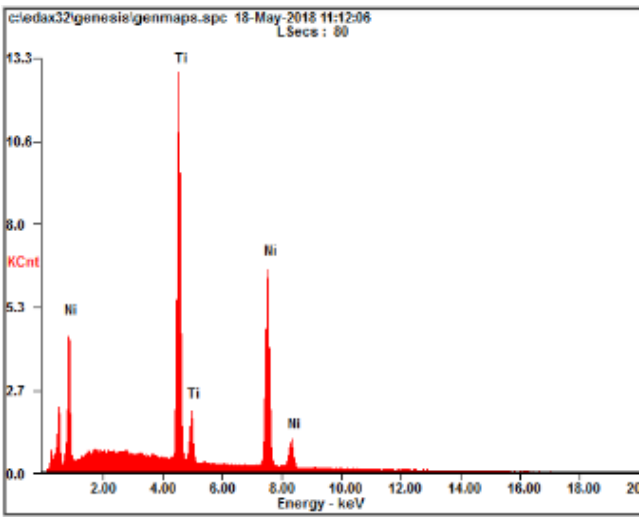

Figure 49. EDS Analysis of Commercial Nitinol Sample

We found multiple references in the literature that indicate that the sample preparation and heating process can greatly influence the composition of the Ni-Ti phases [3], [5], [6]. It is valuable to recognize that the NiTi composition does not need to be exactly 50–50at% in order to exhibit shape memory effects, as shown in the Nitinol, but the composition needs to be close enough to the desired percentage as depicted in the NiTi phase diagram.

Nitinol typically experiences an endothermic phase transformation from martensite to austenite during heating and the reverse exothermic austenite to an intermediate R phase (trigonal martensite) and then R phase to martensite transition during the cooling cycle [34]. To determine the transformation temperatures range for SMAs, our sample and commercial Nitinol were compared using DSC to validate the existence of SME as illustrated in Figure 50. Both samples were thermally cycled twice starting at approximately 30ºC, raised to 100º C and then decreased back to 30º C. The heating and cooling rates were set to 5ºC per minute. During the cycles, the DSC overshot the desired maximum temperature to 107ºC and did not reach the desired lower temperature (reaching only a minimum of 47ºC), so the reliability of the reverse reaction was not discussed. The results for the first cycle indicated the commercial Nitinol wire had a large peak starting at 55ºC with a maximum endothermic reaction at 64ºC and ending at 80ºC. The sample shows

a gradual peak starting at the same temperature of 55ºC, but peaked at 80ºC and continued until 102ºC. The endothermic reactions of Nitinol wire and the sample were measured using the area of the curves with 179.2 and 110.8 µVs, respectively. The differences between the two samples might be related to the phases formed during the heating processes and the wide range of compositions encountered.

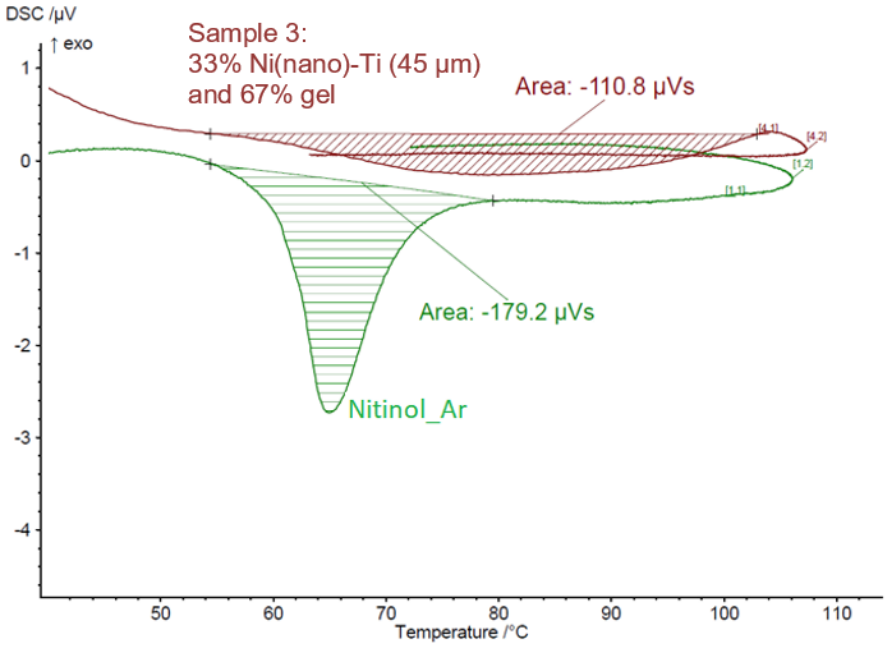

Figure 50. DSC Comparison of Commercial Nitinol Wire and Sample Containing 33% Ni (nano)-Ti (45 µm) and 67% Gel

The single transformation shows an endothermic reaction which correlates with the energy of the martensitic to austenitic transformation. This transition occurs during the heating cycle. However, transformations to the martensitic phase were not observed during the cooling cycles of the DSC test. This could possibly be affected by the heating and cooling rates, making the peaks non-differentiable and the unknown cold worked state of the sample. Also, the desired minimum temperature never actually reached 30°C, so this could have a significant impact on the martensitic transformation phase.

It is also important to note that the separation of the endothermic and exothermic peaks indicate the presence of R phase [34]. In our case, R phase was not observed during

heating or cooling cycles. Based on our fabrication conditions, it would not be expected to identify an R phase transition given that samples were sintered at 1000ºC and multiple annealing cycles are necessary to produce the phase and the SMA effect. Since the initial sample did not have any existing R phase, no transition was detected. As previously mentioned, the microstructures detected in this work are similar to the ones generated in commercial specimens, having the potential to present SMA effect if several thermal cycles were conducted. In overall, the comparison of the commercial Nitinol wire and the sample demonstrated an existence of a correlating endothermic reaction and possible existence of a shape memory effect.

2. Hot Isostatic Pressing

HIP method was then considered to reduce the porosity and retain the geometry of the final parts. HIP service contract was created with AIP to accomplish the work. Table 5 (from Chapter II, Section A.3.b) lists the samples containing different compositions and treated at various HIP conditions.

Two samples, consisting of Ni (5 μm), Ti (45 μm) and gel, were 3D printed as seen in Figure 51, and were left to dry overnight before sending them for a HIP service. They were non-sintered green states, so special handling was necessary to prevent damaging the samples.

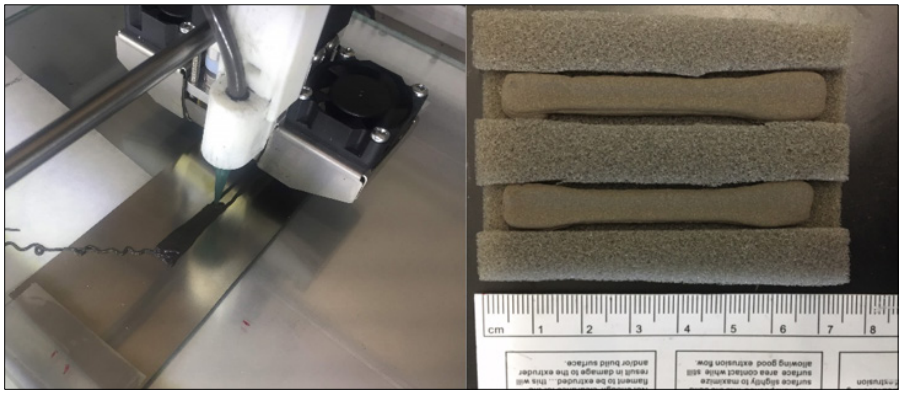

Figure 51. 3D Printed Samples Containing Ni (5 μm), Ti (45 μm) and Gel

All specimens were HIPped and returned as presented in Figure 52. They were subjected to sintering at 1000°C for three hours under argon environment. One specimen was treated under pressure at 138 MPa (20,000 psi) while the other specimen was treated at 172 MPa (25,000 psi) as noted in Figure 52. The returned specimens were already broken in several spots showing some signs of shrinkage, as it is commonly seen in other power metallurgy fabrication approaches. However, they successfully achieved near net shapes in comparison with the furnace samples in the previous section.

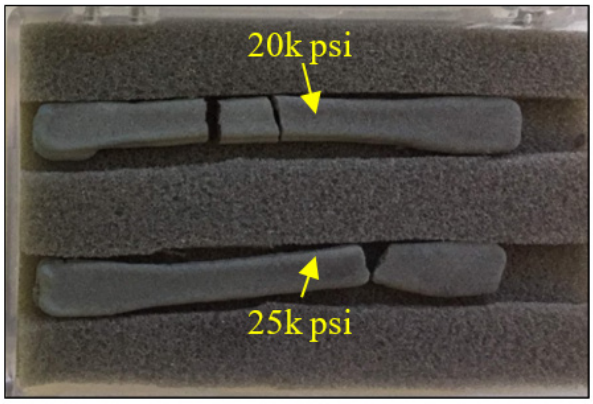

Figure 52. Returned HIPped Samples
Containing Ni (5 μm), Ti (45 μm) and Gel

To better evaluate the porosity of the samples, a small section of each specimen was cold mounted, as demonstrated in Figure 53, to provide flat polished surface that can be examined under SEM and optical microscope at the microstructural level. The SEM images of both specimens in Figure 54 were taken from the center view at a magnification of 300x, showing that the particles sintered together. However, the specimen treated at 138 MPa (20k psi) exhibited larger pores than the specimen treated at higher pressure of 172 MPa (25k psi). The darker areas represent the pores that embedded between the sintered particles as pointed out in the image.

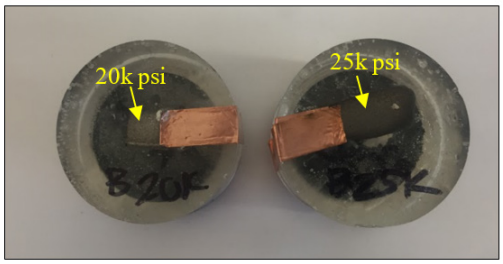

Figure 53. Cold-Mounted HIPped Samples Containing Ni (5 µm), Ti (45 µm) and Gel Treated at Pressure: 138 and 172 MPa (20k and 25k psi)

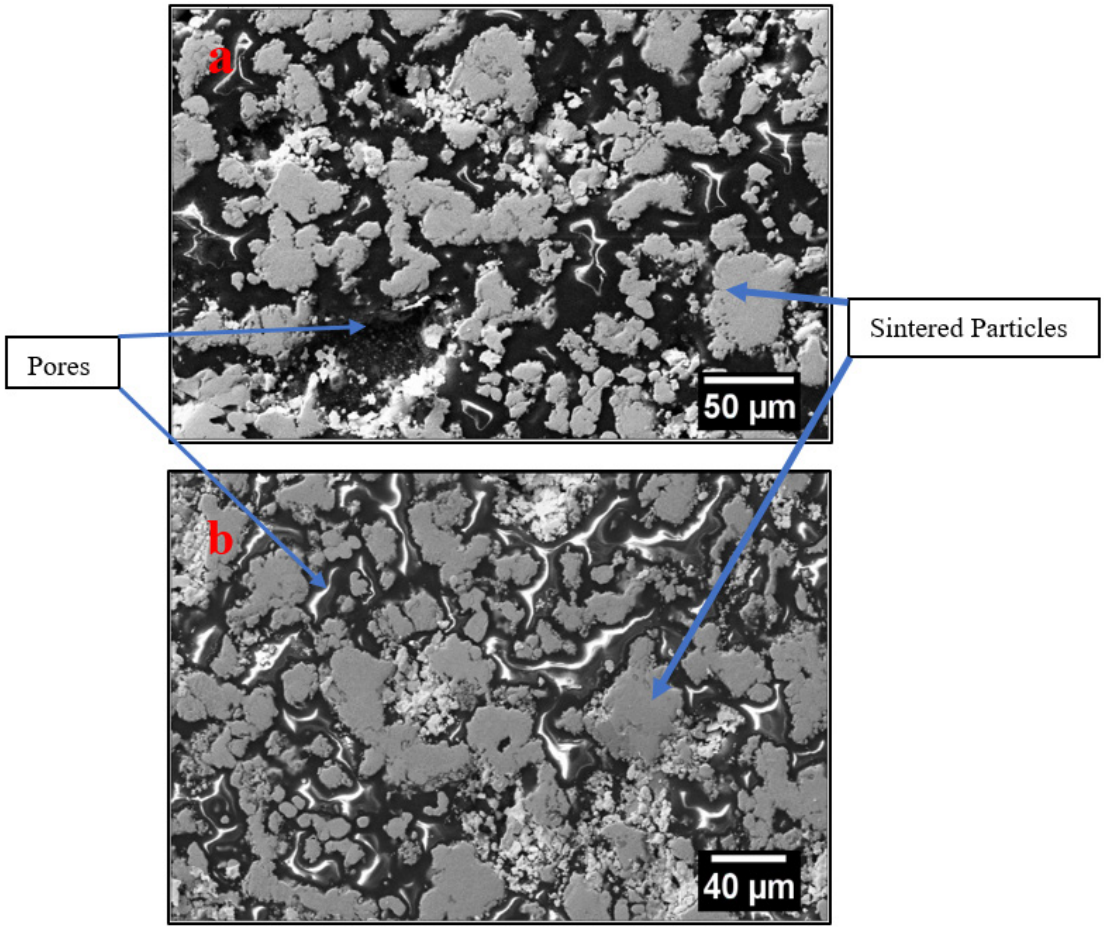

Figure 54. SEM Images of HIPped Samples Containing Ni (5 µm), Ti (45 µm) and Gel Treated at Pressure of (a) 138 MPa, (b) 172 MPa

Both specimens were observed under an optical microscope at the magnification of 2.5x, capturing the raw images of the samples. The imaging processing software, ImageJ,

[35] was then utilized to convert the raw image pixels to binary bits and measure the porosity of the HIPped samples. Figure 55 and 56 present the images of the samples treated at pressure of 138 and 172 MPa, respectively. The sample containing Ni (5 µm), Ti (45 µm) and gel that was treated at 138 MPa resulted in the porosity of 15% while the other sample treated at 172 MPa had the porosity of 3%. The differences in the porosity level suggest that the porosity of the NiTi sample was significantly reduced at a higher pressure (172 MPa psi in this case) than the sample treated at a lower pressure (138 MPa).

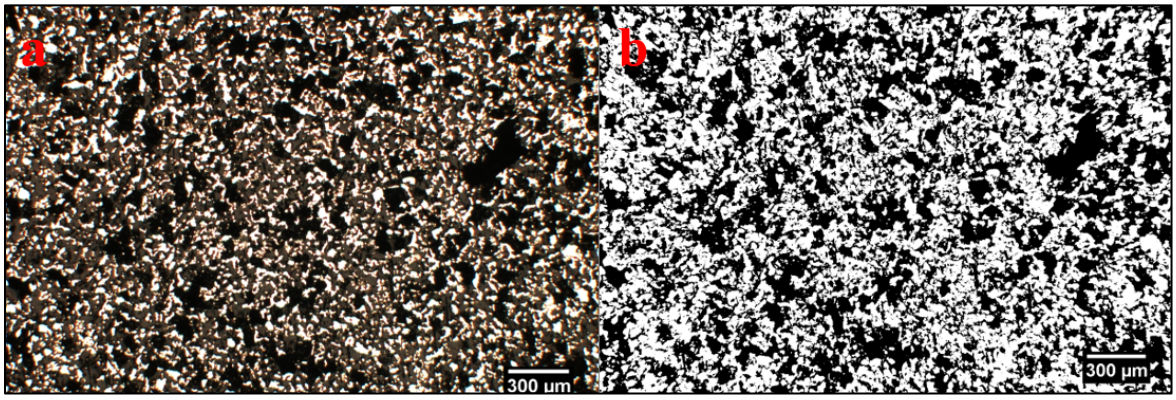

Figure 55. Sample Containing Ni (5 µm), Ti (45 µm) and Gel Treated at 138 MPa in (a) Raw Optical Image and (b) Binary Image

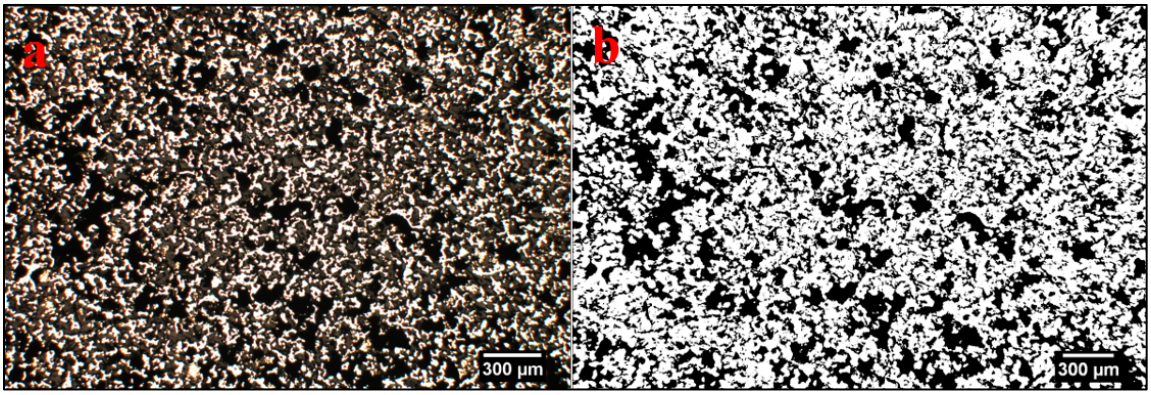

Figure 56. Specimen Treated at 172 MPa in (a) Raw Optical Image and (b) Binary Image

Figure 57 presents SEM images of the samples treated at 138 and 172 MPa respectively, showing the segregation of the diverse Ni-Ti phases.

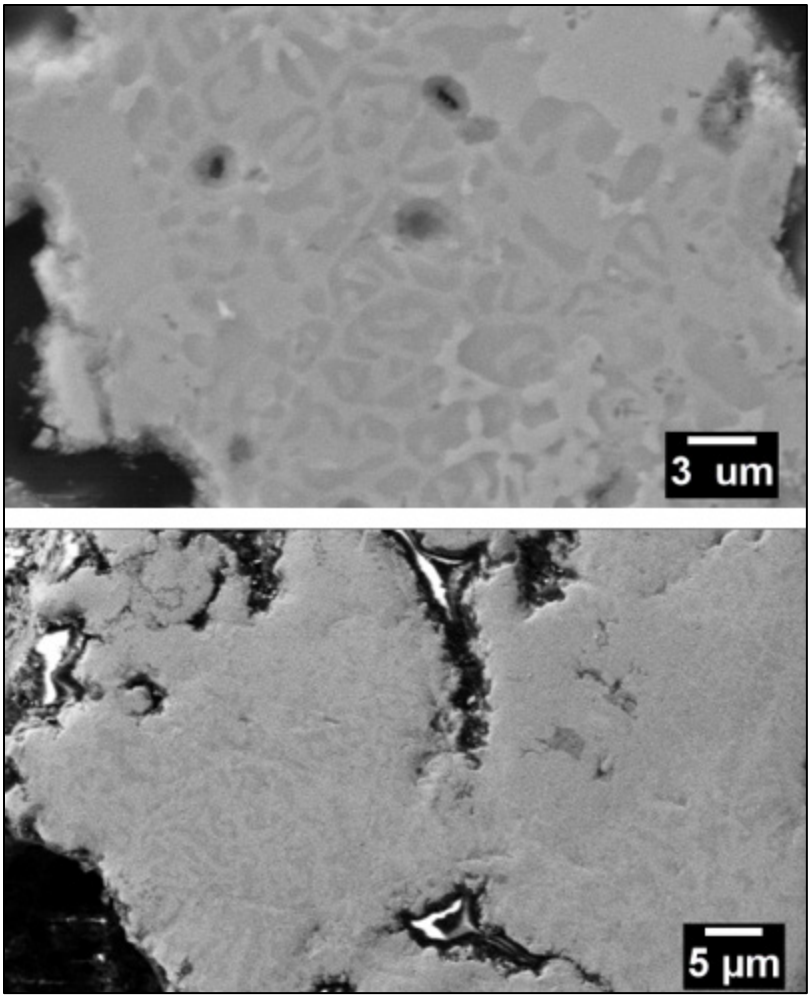

Figure 57. SEM Image of HIPped Samples Treated at 138 MPa (top) and 172 MPa (bottom)

The first set of HIPped samples were relatively porous as mentioned previously, thus we proposed to incorporate carbon nanotubes (CNT) into the paste formulations in an effort to improve the sintering. We proceeded with 3D printing the last samples containing CNTs, Ni (5 µm), Ti (45 µm) and gel, and the samples were then HIPped at 1000°C for five hours under pressure of 207 MPa (30,000 psi), as shown in Figure 58. Given the increased viscosity of the mixture and the difficulties of 3DP a paste containing CNTs, the amount of gel used in the paste formulations was increased by 2 grams. This mixture contained 70mg of CNTs, a small quantity that still affected the viscosity of the mixture significantly. For this reason, we chose to use only a small amount of CNTs needed to

create an adequate paste for 3DP. As seen in the right image, the HIPped samples also suffered the shrinkage as observed in the previous samples.

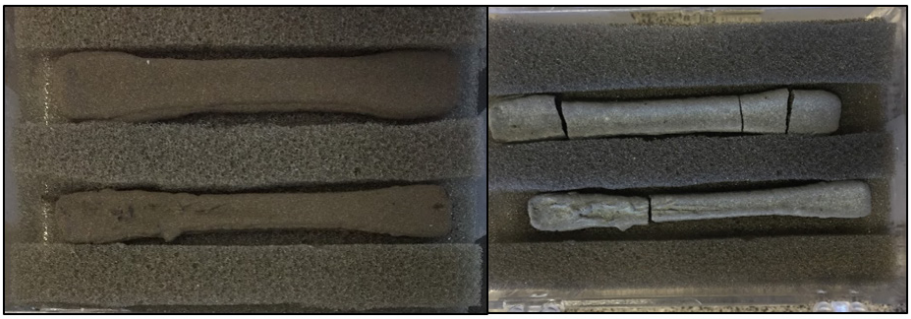

Figure 58. Samples Containing CNTs, Ni (5 μm), Ti (45 μm) and gel Prior to (left) and After HIPped at 207 MPa (right)

A small section of the sample was mounted in resin and polished, as illustrated in Figure 59. The SEM analysis was performed on the samples in different magnifications to evaluate their microstructural characteristics, Figure 60. The particles in the samples sintered together, but the void spaces between the agglomerated particles remained apparent. The sharp-looking spikes represented by the CNTs formed larger agglomerations than the areas without CNTs, which could explain the possibility that CNTs do enhance the sintering. The porosity in the sample remained an issue, but this could be affected by the increase of the gel used in the paste formulations. According to Yuan et al., the porosity of the NiTi SMAs can be controlled by modifying the processing parameters, such as hot pressure, heating rate, mold pressure and cold pressure [36]. His work suggested that by increasing the heating rate during the HIP process it can substantially increase the porosity of the samples. The heating rate used were 17 and 30℃/min with a hot pressure of about 152 MPa (22k psi) and sintering temperature of 1050℃ for three hours. However, his experiment consisted of nickel and titanium powders mixture only. In their case, there was no binding agent used and they utilized mold pressure to produce green samples. His results showed that the sample with the heating rate of 17℃/min had porosity of 38.9% and the highest porosity of 77.6% heated at the rate of 30℃/min. In comparison to our findings,

our samples were HIPped at a much lower heating rate of 10°C/min. This could also explain why the porosity of our samples were significantly lower than what he obtained.

Figure 59. Prepared Sample Containing CNTs, Ni (5 µm), Ti (45 µm) and Gel Treated at 207 MPa for Characterization

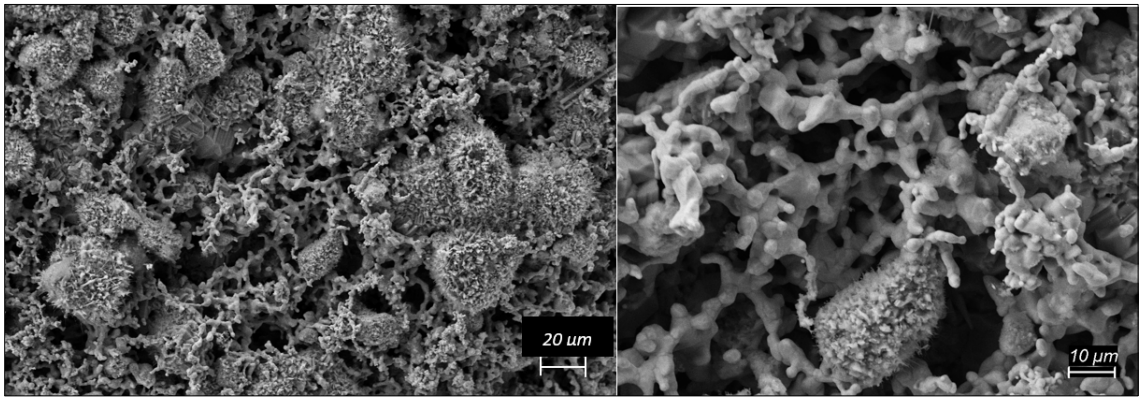

Figure 60. SEM Images of HIPped Sample Containing CNTs, Ni (5 µm), Ti (45 µm) and Gel at Magnification of 300X (left) and 1000X (right)

THIS PAGE INTENTIONALLY LEFT BLANK

IV. CONCLUSION

This final chapter summarizes the overall milestones that were accomplished in this thesis research in both the fabrication and materials characterization processes. It also presents conclusions regarding the research objectives and the recommendations for future works.

A. MILESTONES ACHIEVED

It was determined that the commercial PLA infused with metal particulates was ineffective in producing metals or alloys with the necessary mechanical robustness. All the infused samples of PLA with metal particulates presented lower tensile strengths (TS) than bare PLA. Also, when burning off the polymer it tends to oxidize the particles or leave carbon behind.

The semi-solid paraffin was not a good candidate for the binding agent because it cannot be burned off cleanly without modifying the composition of the sample. Under nitrogen atmosphere and high temperatures, the alloy contains traces of TiN. In argon environment, the alloy contains traces of carbide. Any byproduct of the organic paraffin binder decomposition is unwanted because it can compromise the structural integrity and mechanical strength of the metal alloys.

The binding agent (the alcohol-based gel) was suitable in creating a paste with metal particles. The gel exhibits the appropriate viscosity for 3DP process and most significantly, it can be evaporated easily without modifying the composition or leaving residues in the sample.

Reducing the amount of gel used in the paste formulations also promotes the pores reduction significantly. But, doing so would also affected the ease and effectiveness of 3DP process because the paste becomes more viscous and in general, more resistant to flow. However, it was determined that the minimum amount of gel (50% ratio with respect to NiTi powders) was needed to generate a paste formulation that allows for easy and uniform flow throughout the 3DP process. Through this process, it was demonstrated that it is

possible to 3D print Ni-Ti pastes using a modified polymeric printer, such as the Ultimaker 2+ printer.

Ni nanoparticles behave as shear-thinning fluids (a type of non-Newtonian fluid behavior) when mixed with the gel. Despite the increased amount of Ni (nano) powder added to the formulation, it failed to thicken the substance and overall the viscosity was too low to 3D print a part. In contrast with Ni-micron particles, they behaved closely to a Newtonian fluid and the flow properties of NiTi pastes were much more adequate for 3D printing.

The particles could be sintered successfully at a temperature of 1000℃ for a minimum of 5 hours and at 21 hours at maximum. The sintering process and cooling must be conducted in an argon atmosphere to preclude significant oxidation in the samples.

It was found that subjecting the green samples to hot isostatic pressing can retain the shape of the geometry more effectively than what the conventional furnace treatment can do. The HIPped samples did not shrink significantly when comparing to those treated in a furnace. Additionally, increasing the HIP pressure can help reducing the porosity of the sample as well.

The desired 50–50at% NiTi is not necessarily required to achieve shape memory effects, but the composition should be as close as possible to the desired percentage. It was demonstrated that the chemical compositions of our fabricated NiTi sample was 41–59wt% Ni-Ti, which are outside the ideal band for shape memory effects (55-50wt% Ni-Ti) based on the Ni-Ti phase diagram. However, the sample still showed existence of endothermic reaction and possible existence of SME. It was acknowledged that even with the commercial Nitinol, the ratios of the compositions also fall outside the ideal band for SME, a 61–39wt% Ni-Ti, but the Nitinol wire still exhibited SME when tested.

In sum, this work proves that it is possible to produce 3D parts from pastes containing Ni and Ti micron-sized particulates using a low cost polymeric printer.

B. FUTURE DIRECTIONS

While there were significant milestones accomplished in this study, the possibility for future advancement in the fabrication of SMAs using AM and post-processing routes was recognized.

Recently, the Mechanical Engineering department has received a new 3D bioprinter (r3bel mini), which is built by the SE3D company and funded by a National Science Foundation (NSF), developing solely on bioprinting technology. The printer is available for NPS research students to use for their study in additive manufacturing field. This printer holds promises in the ease of usage and effectiveness of 3DP process; it eliminates the need for plastic tubing because the paste would be delivered directly from the syringe onto the build plate. The first recommendation is to initially experiment with this new printer and see if it performs more effectively than the conventional polymeric printer (Ultimaker 2+ printer). The second recommendation is to further investigate the 3DP process. For instance, allowing each layer to dry before adding another layer could potentially improve the porosity of the printed sample. The third recommendation is to conduct multiple annealing cycles in the printed sample to produce the R phase during the heating and cooling cycles, as seen in a typical DSC thermogram of Nitinol. Lastly, it would also be valuable to find an effective approach to incorporate Ni nanoparticles in the paste without causing the fluid to be too high in viscosity. Solving this problem could potentially improve the sintering characteristics and increase the mechanical robustness of the final products while retaining the unique properties of the nanomaterial integrated in the printed materials.

THIS PAGE INTENTIONALLY LEFT BLANK

LIST OF REFERENCES

[1] Z. Rahman, S. F. Barakh Ali, T. Ozkan, N. A. Charoo, I. K. Reddy, and M. A. Khan, "Additive manufacturing with 3D printing: progress from bench to bedside," *AAPS J.*, vol. 20, no. 6, Nov. 2018. [Online]. https://doi.org/10.1208/s12248-018-0225-6

[2] D. Lehmhus, M. Busse, A. von Hehl, and E. Jägle, "State of the art and emerging trends in additive manufacturing: from multi-material processes to 3D printed electronics," *MATEC Web Conf.*, vol. 188, p. 03013, 2018. [Online]. https://doi.org/10.1051/matecconf/201818803013

[3] M. Elahinia, N. S. Moghaddam, M. T. Andani, A. Amerinatanzi, B. A. Bimber, and R. F. Hamilton, "Fabrication of NiTi through additive manufacturing: A review," *Prog. Mater. Sci.*, vol. 83, pp. 630–663, Oct. 2016. [Online]. https://doi.org/10.1016/j.pmatsci.2016.08.001

[4] P. Kocovic, *3D Printing and Its Impact on the Production of Fully Functional Components: Emerging Research and Opportunities*. Hershey, PA: IGI Global, 2001. [Online]. Available: https://www-igi-global-com.libproxy.nps.edu/gateway/book/173026

[5] H. Sina, S. Iyengar, and S. Melin, "Sintering and reaction behaviour in Ni-Ti powder mixtures," in *Advances in powder metallurgy & particulate materials - 2012: proceedings of the 2012 International Conference on Powder Metallurgy & Particulate Material: PowderMet 2012,* June 10–13, Nashville, 2012, vol. 5, p. 05. [Online]. Available: http://lup.lub.lu.se/record/3971547

[6] M. Bram, A. Ahmad-Khanlou, A. Heckmann, B. Fuchs, H. P. Buchkremer, and D. Stöver, "Powder metallurgical fabrication processes for NiTi shape memory alloy parts," *Mater. Sci. Eng. A*, vol. 337, no. 1–2, pp. 254–263, Nov. 2002. [Online]. https://doi.org/10.1016/S0921-5093(02)00028-X

[7] N. Sharma, K. K. Jangra, and T. Raj, "Fabrication of NiTi alloy: a review," *Proc. IMechE*, vol. 232, no. 3, pp. 250–269, 2018. [Online]. https://doi.org/10.1177/1464420715622494

[8] D. Gu, "Laser additive manufacturing (AM): classification, processing philosophy, and metallurgical mechanisms," in *Laser Additive Manufacturing of High-Performance Materials*, D. Gu, Ed. Berlin, Heidelberg: Springer Berlin Heidelberg, 2015, pp. 15–71. [Online]. https://doi.org/10.1007/978-3-662-46089-4_2

[9] G. S. Altug-Peduk, S. Dilibal, O. Harrysson, S. Ozbek, and H. West, "Characterization of Ni–Ti alloy powders for use in additive manufacturing," *Russ. J. Non-Ferr. Met.*, vol. 59, no. 4, pp. 433–439, Jul. 2018. [Online]. https://doi.org/10.3103/S106782121804003X

[10] K. Otsuka and C. M. Wayman, *Shape Memory Materials*. United Kingdom: Cambridge University Press, 1999.

[11] I. Mihálcz, "Fundamental characteristics and design method for nickel-titanium shape memory alloy," *Period. Polytech. Mech. Eng.*, vol. 45, no. 1, pp. 75–86, 2001. [Online]. Available: https://pp.bme.hu/me/article/view/1410

[12] W. Huang, "Shape memory alloys and their application to actuators for deployable structures," Ph. D dissertation, Dept. of Engineering, University of Cambridge, UK, 1998. [Online]. Available: http://www3.ntu.edu.sg/home/mwmhuang/cambridge/Phd2side.pdf

[13] S. George, "Shape memory alloys," Slideshare, February 16, 2016. [Online]. Available: https://www.slideshare.net/sajithnbg/shape-memory-alloys-58329620

[14] W. B. Cross, A. H. Kariotis, and F. J. Stimler, "Nitinol characterization study," Goodyear Aerospace Corporation, Akron, OH, USA, Rep. GER14188, 1969. [Online]. Available: https://ntrs.nasa.gov/archive/nasa/casi.ntrs.nasa.gov/19690026989.pdf

[15] K. Otsuka and X. Ren, "Physical metallurgy of Ti–Ni-based shape memory alloys," *Prog. Mater. Sci.*, vol. 50, no. 5, pp. 511–678, Jul. 2005. [Online]. https://doi.org/10.1016/j.pmatsci.2004.10.001

[16] P. Duwez and J. L. Taylor, "The structure of intermediate phases in alloys of titanium with iron, cobalt, and nickel," *JOM*, vol. 2, no. 9, pp. 1173–1176, Sep. 1950. [Online]. https://doi.org/10.1007/BF03399120

[17] M. Mokgalaka, S. Pityana, P. Popoola, and T. Mathebula, "NiTi intermetallic surface coatings by laser metal deposition for improving wear properties of Ti-6Al-4V substrates," *Adv. Mater. Sci. Eng.*, vol. 2014, pp. 1–8, Mar. 2014. [Online]. https://doi.org/10.1155/2014/363917

[18] G. Costanza and M. E. Tata, "A novel methodology for solar sail opening employing shape memory alloy elements," *J. Intell. Mater. Syst. Struct.*, vol. 29, no. 9, pp. 1793–1798, May 2018. [Online]. https://doi.org/10.1177/1045389X17754262

[19] TiNi Aerospace, “Frangibolt,” Accessed November 1, 2018. [Online]. Available: https://tiniaerospace.com/products/space-frangibolt/

[20] P. Harkness, M. McRobb, P. Lützkendorf, R. Milligan, A. Feeney, and C. Clark, “Development status of AEOLDOS – a deorbit module for small satellites,” *Adv. Space Res.*, vol. 54, no. 1, pp. 82–91, Jul. 2014. [Online]. https://doi.org/10.1016/j.asr.2014.03.022

[21] O. Ivanova, C. Williams, and T. Campbell, “Additive manufacturing (AM) and nanotechnology: promises and challenges,” *Rapid Prototyp. J.*, vol. 19, p. 353, Jul. 2013. [Online]. https://doi.org/10.1108/RPJ-12-2011-0127

[22] Sasol. “Material safety data sheet-petroleum jelly,” November 4, 2011. [Online]. Available: https://www.sasol.com/online-store/sites/default/files/datasheets/safety_data_sheet_11-04-2011_1.pdf

[23] Gojo. “Safety data sheet- PURELL® hand sanitizer gel,” February 10, 2015. [Online]. Available: http://sds.staples.com/msds/633539.pdf

[24] Autodesk. “Fusion 360.” Accessed November 6, 2018. [Online]. Available: https://www.autodesk.com/products/fusion-360/students-teachers-educators

[25] Ultimaker. “Ultimaker Cura software.” Accessed November 6, 2018. [Online]. Available: https://ultimaker.com/en/products/ultimaker-cura-software

[26] G. Cao, *Nanostructures & Nanomaterials: Synthesis, Properties & Applications;* London: Imperial College Press, 2004.

[27] M. Theresa, “Scanning electron microscope (sem),” Slideshare, March 31 2017. [Online]. Available: https://www.slideshare.net/MaryTheresa4/scanning-electron-microscope-sem-74020395

[28] T. W. Duerig, A. R. Pelton, and K. Bhattacharya, “The measurement and interpretation of transformation temperatures in nitinol,” *Shape Mem. Superelasticity*, vol. 3, no. 4, pp. 485–498, Dec. 2017. [Online]. https://doi.org/10.1007/s40830-017-0133-0

[29] C. Marchand, A. Maître, A. Grimaud, A. Denoirjean, and P. Lefort, “Nitridation of Ti–6Al–4V powder in thermal plasma conditions and sintering of obtained TiN powder,” *Surf. Coat. Technol.*, vol. 201, no. 5, pp. 1988–1994, Oct. 2006. [Online]. https://doi.org/10.1016/j.surfcoat.2006.04.041

[30] J. H. Abboud, A. F. Fidel, and K. Y. Benyounis, “Surface nitriding of Ti–6Al–4V alloy with a high power CO2 laser,” *Opt. Laser Technol.*, vol. 40, no. 2, pp. 405–414, Mar. 2008. [Online]. https://doi.org/10.1016/j.optlastec.2007.07.005

[31] Renishaw Plc, “Investigating the effects of multiple powder re-use in AM: additive manufacturing titanium Ti6Al4V alloy AM250 ageing study,” Renishaw Plc., Staffordshire, UK, H-5800-3384-01-A, 2016. [Online]. Available: https://resources.renishaw.com/en/details/White%20paper%3a%20%20Investigating%20the%20effects%20of%20multiple%20powder%20re-use%20in%20AM(83164)

[32] W. J. Tseng and C.-N. Chen, “Dispersion and rheology of nickel nanoparticle inks,” *J. Mater. Sci.*, vol. 41, no. 4, pp. 1213–1219, Feb. 2006. [Online]. https://doi.org/10.1007/s10853-005-3659-z

[33] Z. Wu, A. Mahmud, J. Zhang, Y. Liu, and H. Yang, “Surface oxidation of NiTi during thermal exposure in flowing argon environment,” *Mater. Des.*, vol. 140, pp. 123–133, 2018. [Online]. https://doi.org/10.1016/j.matdes.2017.11.061

[34] J. Uchil, K. K. Mahesh, and K. Ganesh Kumara, “Calorimetric study of the effect of linear strain on the shape memory properties of Nitinol,” *Phys. B Condens. Matter*, vol. 305, no. 1, pp. 1–9, Oct. 2001. [Online]. https://doi.org/10.1016/S0921-4526(01)00593-2

[35] C. Rueden, “Introduction,” ImageJ, June 17, 2014. [Online]. Available: https://imagej.net/Introduction

[36] B. Yuan, M. Zhu, Y. Gao, X. Li, and C. Y. Chung, “Forming and control of pores by capsule-free hot isostatic pressing in NiTi shape memory alloys,” *Smart Mater. Struct.*, vol. 17, no. 2, p. 025013, Apr. 2008. [Online]. https://doi.org/10.1088/0964-1726/17/2/025013

INITIAL DISTRIBUTION LIST

1. Defense Technical Information Center
   Ft. Belvoir, Virginia

2. Dudley Knox Library
   Naval Postgraduate School
   Monterey, California